Article

Immunity

Targeting Degradation of the Transcription Factor C/EBPβ Reduces Lung Fibrosis by Restoring Activity of the Ubiquitin-Editing Enzyme A20 in Macrophages

Graphical Abstract

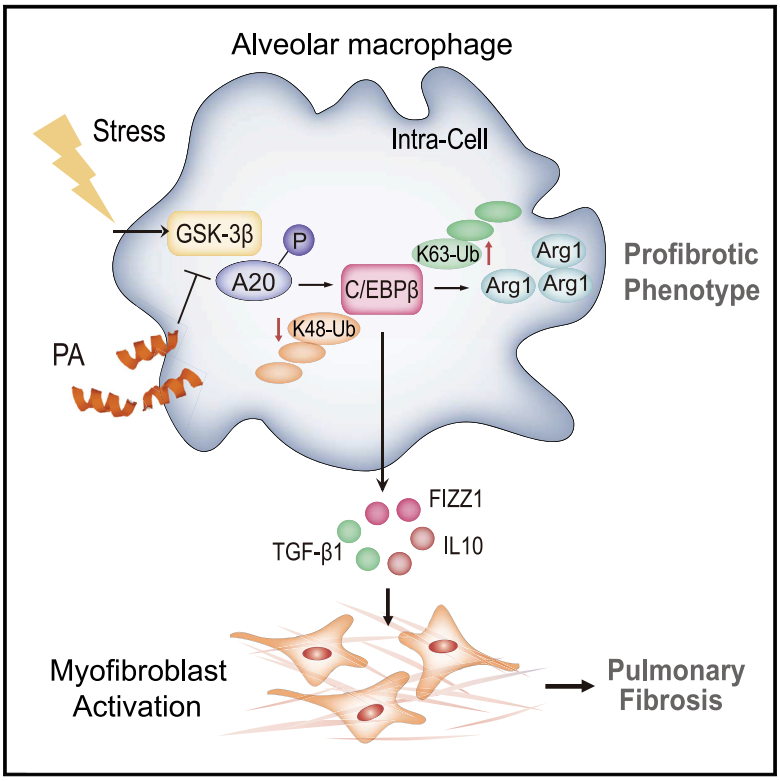

Authors

Shan-shan Liu, Xiao-xi Lv, Chang Liu, ..., Xia Li, Bo Huang, Zhuo-wei Hu

Correspondence

huzhuowei@imm.ac.cn

In Brief

Dysregulation of the ubiquitin-editing enzyme A20 contributes to the development of several human inflammatory diseases. Liu et al. demonstrate that suppression of A20 enzymatic activity in alveolar macrophages promotes lung fibrosis by reducing transcriptional factor C/EBPβ degradation and enhancing targeted gene expression, which directs the profibrotic phenotype of macrophages.

Highlights

- A20 activity in alveolar macrophages negatively correlates with lung fibrosis
- A20 exerts its anti-fibrotic activities by destabilizing C/EBPβ in AMs
- GSK-3β interacts with and phosphorylates A20 to impede its activity
- Targeting GSK-3β/A20 interaction reduces lung fibrosis by degrading C/EBPβ

Liu et al., 2019, Immunity *51*, 1–13
September 17, 2019
https://doi.org/10.1016/j.immuni.2019.06.014

CellPress

Please cite this article in press as: Liu et al., Targeting Degradation of the Transcription Factor C/EBPβ Reduces Lung Fibrosis by Restoring Activity of the Ubiquitin-Editing Enzyme A20 in Macrophages, Immunity (2019), https://doi.org/10.1016/j.immuni.2019.06.014

Targeting Degradation of the Transcription Factor C/EBPβ Reduces Lung Fibrosis by Restoring Activity of the Ubiquitin-Editing Enzyme A20 in Macrophages

Shan-shan Liu,[1,7] Xiao-xi Lv,[1,7] Chang Liu,[1] Jie Qi,[2] Yun-xuan Li,[1] Xu-peng Wei,[3] Ke Li,[4] Fang Hua,[1] Bing Cui,[1] Xiao-wei Zhang,[1] Jiao-jiao Yu,[1] Jin-mei Yu,[1] Feng Wang,[1] Shuang Shang,[1] Chen-xi Zhao,[1] Xue-ying Hou,[1] Zhi-gang Yao,[5] Ping-ping Li,[1] Xia Li,[2] Bo Huang,[6] and Zhuo-wei Hu[1,8,*]

[1]Molecular Immunology and Pharmacology Group, State Key Laboratory of Bioactive Substance and Function of Natural Medicines, Institute of Materia Medica, Chinese Academy of Medical Sciences & Peking Union Medical College, Beijing 100050, China
[2]Department of Pharmacy, Marine College, Shandong University, Weihai 264209, China
[3]Department of Pharmacy, Pharmacy College, Hebei University, Baoding 071000, China
[4]NHC Key Laboratory of Biotechnology of Antibiotics, Institute of Medicinal Biotechnology, Chinese Academy of Medical Sciences & Peking Union Medical College, Beijing 100050, China
[5]Department of Respiratory Medicine, Beijing Friendship Hospital, Capital Medical University, Beijing, 100050, China
[6]Department of Immunology & National Key Laboratory of Medical Molecular Biology, Institute of Basic Medicine, Chinese Academy of Medical Sciences & Peking Union Medical College, Beijing 100005, China
[7]These authors contributed equally
[8]Lead Contact
*Correspondence: huzhuowei@imm.ac.cn
https://doi.org/10.1016/j.immuni.2019.06.014

SUMMARY

Although recent progress provides mechanistic insights into the pathogenesis of pulmonary fibrosis (PF), rare anti-PF therapeutics show definitive promise for treating this disease. Repeated lung epithelial injury results in injury-repairing response and inflammation, which drive the development of PF. Here, we report that chronic lung injury inactivated the ubiquitin-editing enzyme A20, causing progressive accumulation of the transcription factor C/EBPβ in alveolar macrophages (AMs) from PF patients and mice, which upregulated a number of immunosuppressive and profibrotic factors promoting PF development. In response to chronic lung injury, elevated glycogen synthase kinase-3β (GSK-3β) interacted with and phosphorylated A20 to suppress C/EBPβ degradation. Ectopic expression of A20 or pharmacological restoration of A20 activity by disturbing the A20-GSK-3β interaction accelerated C/EBPβ degradation and showed potent therapeutic efficacy against experimental PF. Our study indicates that a regulatory mechanism of the GSK-3β-A20-C/EBPβ axis in AMs may be a potential target for treating PF and fibroproliferative lung diseases.

INTRODUCTION

Many forms of interstitial lung disease (ILD) lead to pulmonary fibrosis (PF), a chronic and progressive pathological change driven by repeated lung injury and inflammation (Putman et al., 2016). Idiopathic pulmonary fibrosis (IPF) is the most common form of ILD, with irreversible PF and a poor clinical outcome. Although pirfenidone and nintedanib have been approved by the US Food and Drug Administration (FDA) to treat IPF, these drugs can only slow the progression of IPF (Richeldi et al., 2017). Thus, understanding the pathogenesis of PF is crucial for the discovery of effective anti-PF drugs. Myofibroblasts are the most important effector cells of PF, producing a large quantity of extracellular matrix (ECM) in the lung alveoli and interstitium (Pardo and Selman, 2016). Myofibroblast differentiation and activation are triggered and maintained by various cytokines and growth factors released from alveolar epithelial and immune cells. Among the immune cells, alveolar macrophages (AMs) are in close proximity to activated myofibroblasts and can trigger chronic inflammation and PF (Wynn and Vannella, 2016). Recently, a number of developmental lineage-tracing studies in mice have shown that an injured lung contains at least two subpopulations of AMs, namely monocyte-derived AMs (Mo-AMs) and tissue-resident AMs (TR-AMs) (McQuattie-Pimentel et al., 2018). Indeed, a number of studies have shown that Mo-AMs that exhibit a proinflammatory and profibrotic phenotype in damaged lung tissue play crucial roles in promoting PF development (McCubbrey et al., 2018; Misharin et al., 2017). However, how Mo-AMs maintain a proinflammatory and profibrotic phenotype and how they contribute to the development of PF remain to be elucidated.

Classically activated macrophages, which are characterized by the secretion of proinflammatory cytokines such as tumor necrosis factor-α (TNF-α), interleukin-1β (IL-1β), and IL-6 are involved in initiating an inflammatory response after tissue injury. In contrast, alternatively activated macrophages, which are characterized by the secretion of anti-inflammatory or immunosuppressive molecules such as IL-4, IL-13, IL-10, and transforming growth factor-β (TGF-β), are involved in the tissue repair and healing process (Gordon, 2003). Notably, the alternatively activated macrophages found in fibrotic tissues are associated

with a profibrotic phenotype (He et al., 2013; Larson-Casey et al., 2016; Mora et al., 2006; Nair et al., 2009; Redente et al., 2014). Thus, manipulating the differentiation of AMs holds therapeutic potential for PF and other fibroproliferative lung diseases.

The ubiquitin-modifying enzyme A20, also known as TNFAIP3, has recently attracted much attention because of its ubiquitin-editing functions and its potent anti-inflammatory ability in diverse human diseases (Ma and Malynn, 2012). These studies have shed light on the molecular mechanisms by which A20 regulates inflammatory signaling cascades, establishing A20 as a crucial gatekeeper in the maintenance of tissue homeostasis. Indeed, A20 plays a role in liver fibrosis, cardiac fibrosis, and cystic fibrosis (Huang et al., 2010; Malcomson et al., 2016; Wang et al., 2017a). However, no evidence has yet shown the role and mechanism of A20 in macrophages in PF development. We thus hypothesized that A20 in AMs regulates the phenotype of AMs and PF development. We examined the expression, activity, and function of A20 in primary AMs from PF mouse models and PF patients and elucidated several functional implications regarding the potential utility of A20 for PF treatment.

RESULTS

A20 in AMs Negatively Correlates with PF Development

To determine the role of A20 in PF development, *Tnfaip3*$^{+/-}$*Lyz2-cre* and *Tnfaip3*$^{F/+}$*Lyz2-cre* mice were generated to enhance or reduce A20 expression in AMs (Figure 1A). Compared with AMs from wild-type (WT) mice, genetically targeted A20 in AMs reduced multiple bleomycin (mBLM)-induced collagen deposition (Figure 1B), Col1 expression (Figure 1C), and hydroxyproline content (Figure 1D) and improved lung function (Figure 1E). However, *Tnfaip3*$^{F/+}$*Lyz2-cre* mice caused much more serious PF changes than WT mice (Figures 1F–1I). Then, we generated *Tnfaip3*$^{+/-}$*Itgax-cre* and *Tnfaip3*$^{F/+}$*Itgax-cre* mice, which resulted in genetically targeted and deficient A20 in AMs (Figures S1A and S1B). Genetically targeting A20 in AMs reduced mBLM-induced PF changes, but deletion of A20 caused much more serious PF changes than those observed in WT mice (Figures S1C and S1D). To ascertain that the anti-PF role of A20 occurred exclusively in AMs, AMs were depleted from mBLM-exposed *Tnfaip3*$^{F/+}$*Lyz2-cre* mice by repetitive intratracheal instillation of clodronate-encapsulated liposomes, which caused selective apoptosis of AMs (Figure 1J). The flow cytometry assay showed that these mice had a 92% reduction of AMs (Figure S1E). AM depletion reduced collagen deposition (Figure 1K) and hydroxyproline content (Figure 1L) but improved lung function (Figure 1M). However, AM depletion induced identical anti-PF changes in WT and *Tnfaip3*$^{F/+}$*Lyz2-cre* mice (Figures 1K–1M). Intratracheal injection of AMs with high purity from mBLM-exposed *Tnfaip3*$^{F/+}$*Lyz2-cre* mice into mice with AM depletion reversed the AM depletion-induced anti-PF changes (Figures 1K–1M). Also, *Tnfaip3*$^{F/+}$*Lyz2-cre* mice that received AMs showed an identical degree of PF changes as WT mice (Figures 1K–1M). Repeated intratracheal instillation of profibrotic AMs induced PF in control mice (Figure S1F). Because several studies have reported the critical role of A20 in lung epithelial cells during allergy and virus infection (Maelfait et al., 2016; Schuijs et al., 2015), *Tnfaip3*$^{+/-}$*Sftpc-cre* mice were generated to overexpress A20 in type 2 epithelial cells (Figure S1G), and these mice showed the same extent of PF changes as those observed in WT mice (Figures S1H and S1I). Notably, overexpression of A20 in mice with the established PF reversed the mBLM-induced fibrotic changes, as indicated by improved lung function (Figures S1J and S1K). These data suggest that the anti-PF effect is exerted exclusively by A20 in AMs.

We examined A20 in which a subpopulation of AMs contributed to PF by sorting TR-AMs and Mo-AMs from the mBLM mouse (Figure S1L). The number of TR-AMs was decreased but the number of Mo-AMs was increased following mBLM exposure (Figure S1M). Also, the number of CD206^{+} Mo-AMs was larger than the number of CD206^{+} TR-AMs from mBLM mouse lungs (Figure S1N). Similarly, CD206 expression in Mo-AMs was much lower in *Tnfaip3*$^{+/-}$*Lyz2-cre* mice than in WT mice (Figure S1O). These data show that A20 in Mo-AMs rather than TR-AMs is critical for PF development (McCubbrey et al., 2018; Misharin et al., 2017).

Enzymatic Dysfunction of A20 in AMs Promotes PF Development

We evaluated A20 expression in AMs from mBLM and control mice. A20 expression was comparable in AMs from mBLM and sham mice (Figures 2A and 2B). However, reduced A20 activity was detected in AMs from mBLM mice (Figure 2C). A20 can restrict K63-linked and/or K48-linked ubiquitination of Traf6, Rip1, and other proteins (Jung et al., 2013; Wertz et al., 2004). The amounts of K63-linked ubiquitinated Traf6 and Rip1 were increased (Figures S1P and S1Q) but the amount of K48-linked ubiquitinated Rip1 was decreased in fibrotic mouse lungs (Figure S1R), suggesting that the enzymatic activity of A20 was impeded with no abundance changes. To investigate why A20 activity in AMs attenuated PF development, single-cell RNA sequencing (scRNA-seq) was performed in AMs from the mBLM-challenged WT and *Tnfaip3*$^{+/-}$*Lyz2-cre* mice (Figure 2D). We sequenced 9,675 cells from WT mice and 12,947 cells from *Tnfaip3*$^{+/-}$*Lyz2-cre* mice. A t-distributed stochastic neighbor embedding (t-SNE) analysis revealed 11 clusters in both WT mice and *Tnfaip3*$^{+/-}$*Lyz2-cre* mice (Figure 2E). However, the relative cell number in each cluster was quite different among groups, indicating that the majority of AMs in *Tnfaip3*$^{+/-}$*Lyz2-cre* mice exhibited distinct transcriptional signatures compared with those in WT mice (Figure 2F). We found that expressions of 231 genes were changed, including the genes encoding immunosuppressive and profibrotic factors such as arginase 1 (Arg1), which were reduced in AMs from *Tnfaip3*$^{+/-}$*Lyz2-cre* mice relative to those from WT mice (Figures 2G and 2H), indicating that genetically targeted A20 abrogated the profibrotic AMs phenotype. AMs from *Tnfaip3*$^{+/-}$*Lyz2-cre* mice co-cultured with fibroblasts suppressed the expression of Col1 and α-SMA as well as the contraction and proliferation of fibroblasts (Figures 2I–2L). These data indicate that A20 enzymatic dysfunction in AMs promotes PF development.

We verified the anti-fibrotic role of A20 in AMs from bronchoalveolar lavage fluid (BALF) of PF patients and age-matched controls (Table S1). No difference in A20 expression was found between AMs from PF patients and controls (Figures 3A and 3B), but reduced A20 activity was detected in AMs from PF patients (Figure 3C). AMs from PF patients were treated with adenovirus (Ad)-*Tnfaip3* to restore A20 activity (Figure 3C), which

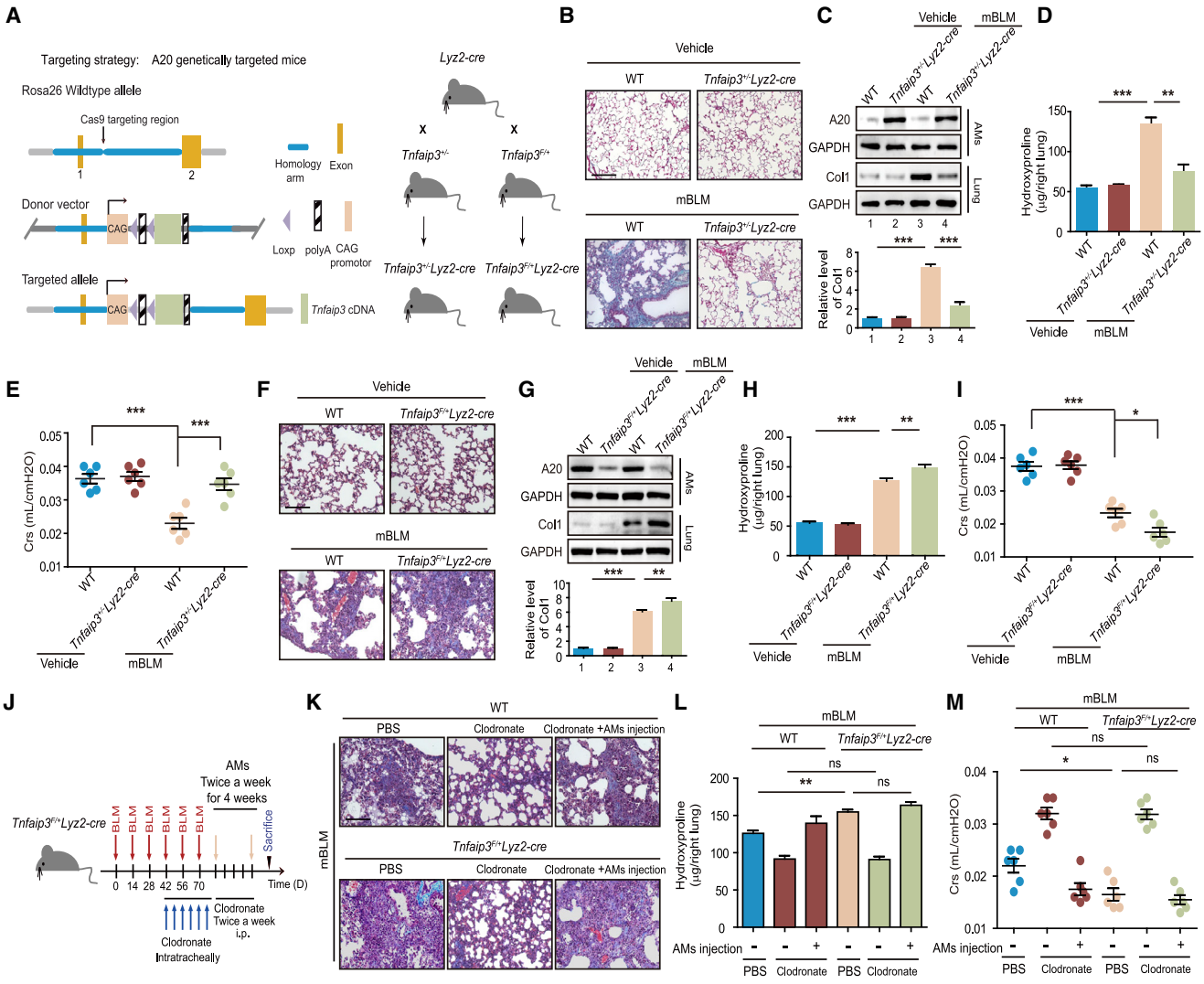

Figure 1. A20 in AMs Negatively Correlates with PF Development

(A) The scheme to generate mice with genetically targeted and deficient A20 in the myeloid cell lineage. These heterozygous *Tnfaip3*$^{+/-}$ and *Tnfaip3*$^{F/+}$ transgenic founder mice were crossed with homozygous *Lyz2-cre* mice. The double-transgenic mice were designated *Tnfaip3*$^{+/-}$*Lyz2-cre* and *Tnfaip3*$^{F/+}$*Lyz2-cre* mice.

(B) Sample images of Masson staining of lung tissues from indicated mice after multiple BLM (mBLM) exposure (n = 6). Scale bars, 200 μm.

(C) The sample blots show A20 expression in AMs and collagen 1 (Col1) expression in lung tissues.

(D) Hydroxyproline content in the lung.

(E) Respiratory system compliance (Crs) in mice.

(F) Sample images of Masson staining of lung tissues from the indicated mice after mBLM exposure. Scale bars, 200 μm.

(G–I) The sample blots show A20 expression in AMs and Col1 expression in lung tissues (G). Hydroxyproline content (H) and Crs (I) were measured to evaluate the lung fibrotic changes.

(J) Strategy for AMs depletion by liposomal clodronate and AMs transfusion intratracheally into mBLM-exposed *Tnfaip3*$^{F/+}$*Lyz2-cre* mice.

(K–M) Masson staining (K), hydroxyproline content in right lung (L), and Crs (M) were performed to evaluate fibrotic changes in lungs. Scale bars, 200 μm.

Statistical significance among groups was determined using one-way ANOVA. Data are representative of two independent experiments of five or six mice per group (mean ± SEM). *p < 0.05, **p < 0.01, and ***p < 0.001. See also Figure S1.

reduced expression of the alternative activated macrophage markers CD206 (Figure 3D) and *TGFB1*, *IL10*, *MRC1*, and *ARG1* (Figure 3E) but upregulated expression of the classical macrophage activation markers *NOS2*, IL1B, and TNF in AMs (Figure 3F). In the AM fibroblast coculture system, A20 overexpression reversed the patients' AM-induced Col1 and α-SMA expression as well as the contraction and proliferation of fibroblasts (Figures 3G–3J). These data indicate that A20 activity in AMs plays a critical role in human PF development.

A20 Suppresses PF by Destabilizing C/EBPβ in AMs

We examined how A20 in AMs produces anti-PF effects. By mass spectrometry identification, 176 proteins were found to bind to A20 in AMs from fibrotic mice but not in those from control mice (Figure 4A). In comparison with 107 proteins that

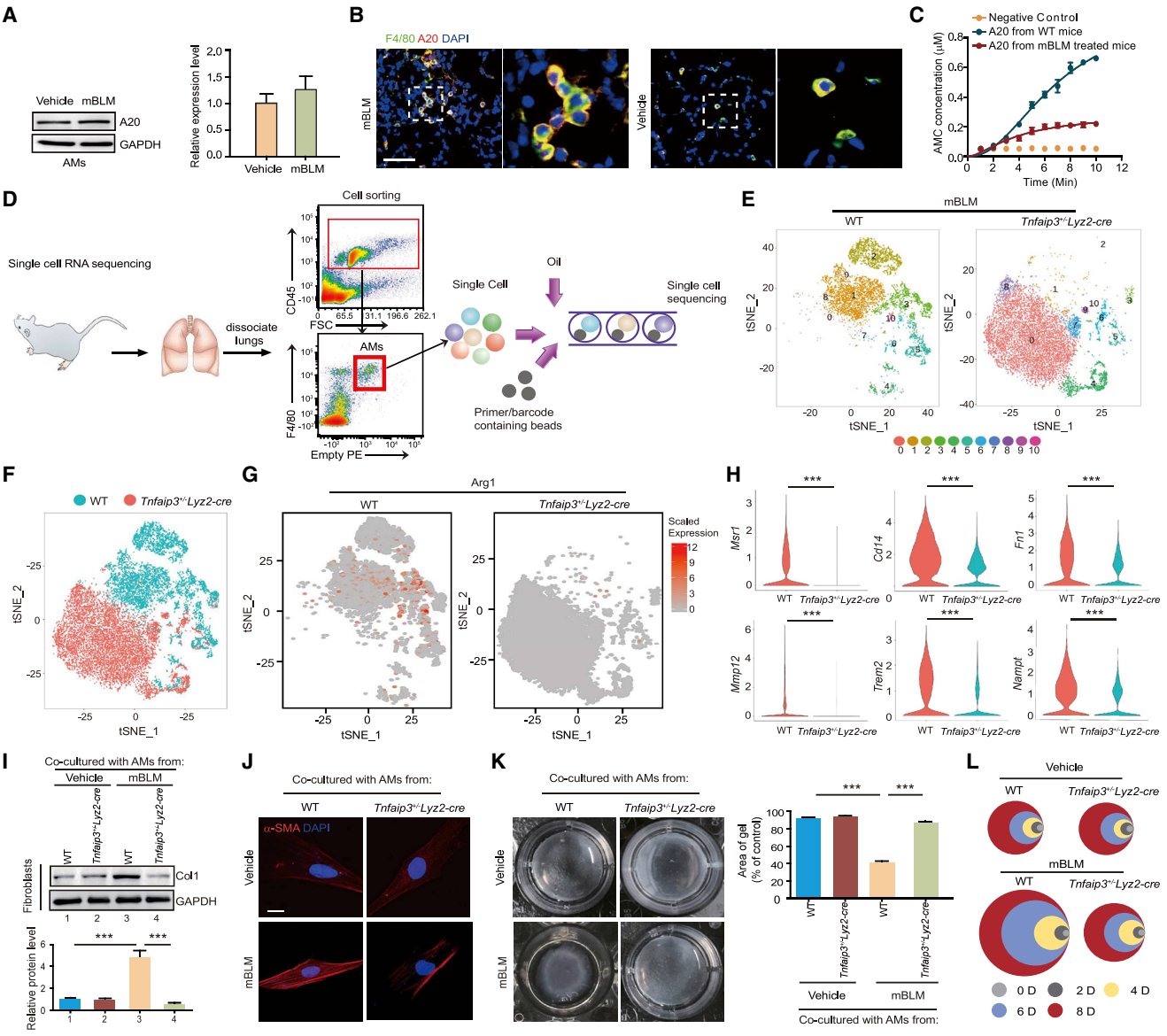

Figure 2. Elevated A20 Activity Inhibits the Profibrotic Phenotype of AMs in Fibrotic Mice

(A) Sample immunoblot images and quantitative analyses of A20 expression in lung tissues from mice at day 10 after mBLM injury. GAPDH was used as a loading control.

(B) Sample confocal images showing A20 expression in AMs from mice at day 10 after mBLM challenge. Scale bars, 50 μm.

(C) A20 protein was IP from AMs in mouse lungs after mBLM exposure. A DUB activity kit was used to test the enzyme activity of A20.

(D) Workflow depicts rapid dissociation and sorting of AMs from lung tissue for generating scRNA transcriptome profiles.

(E) A t-distributed stochastic neighbor embedding (t-SNE) plot of scRNA-seq data of AMs from indicated mice showing clusters.

(F) t-SNE plot depicting AMs from indicated mice.

(G) t-SNE plot showing expression of Arg1 in AMs from the indicated mice at the single-cell level.

(H) Representative violin plots of differentially expressed profibrotic genes in AMs from the indicated mice.

(I–L) AMs isolated from mBLM-exposed WT or *Tnfaip3*$^{+/-}$*Lyz2-cre* mice were co-cultured with primary mouse fibroblasts for the indicated times. The activation of lung fibroblasts was evaluated by the expression of Col1 (I) and α-SMA (J) in primary fibroblasts, fibroblast contractility in three-dimensional collagen matrices (K), and fibroblast proliferation (L). Scale bars, 50 μm.

Statistical significance between two groups was determined using unpaired two-tailed Student's t test; statistical significance among groups was determined using one-way ANOVA. Data are from one experiment representative of two independent experiments (A–C; mean and SEM, n = 5 or 6) or from three independent experiments (I–L; mean and SEM). *p < 0.05, **p < 0.01, and ***p < 0.001. See also Figure S1.

activate AMs reported in the literature, only Stat3, Tbk1, Gab2, and C/EBPβ were found in both groups (Figure 4B). A20 overexpression suppressed only C/EBPβ-induced CD206 expression in AMs (Figure 4C). Additionally, higher C/EBPβ expression was observed in AMs from PF patients than in those from controls (Figures S2A and S2B). A20 overexpression in AMs from

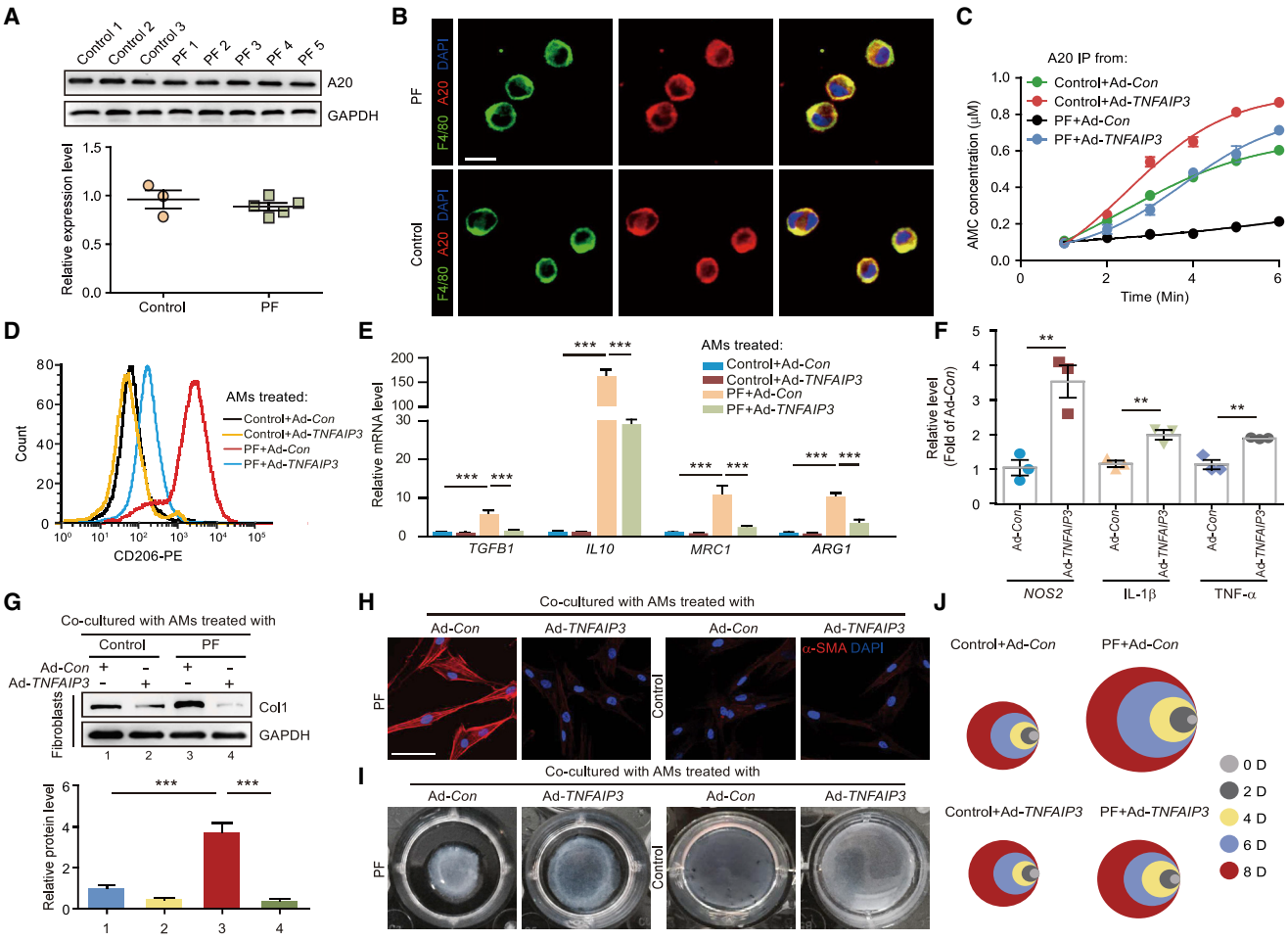

Figure 3. Reduced A20 Activity Directs the Profibrotic Phenotype of AMs from PF Patients

(A) Quantitation of A20 expression in AMs from PF patients (n = 5) or age-matched controls (n = 3). GAPDH was used as a loading control.

(B) Sample confocal images showing A20 expression in AMs from controls or PF patients. Scale bars, 20 μm.

(C) AMs isolated from controls or PF patients were treated with Ad-*TNFAIP3* virus. A20 protein was immunoprecipitated from these cells, and A20 activity was evaluated.

(D) Flow cytometry analyses of CD206 expression in *TNFAIP3*-overexpressed AMs from controls or PF patients.

(E) Quantitative analyses of mRNA of the indicated genes in AMs from controls or PF patients.

(F) Quantitative analyses of *NOS2* mRNA by RT-PCR and cytokine content of TNF-α and IL-1β by ELISA in human AMs from PF patients infected with Ad-*Con* or Ad-*TNFAIP3* virus.

(G–J) Human AMs were infected with Ad-*Con* or Ad-*TNFAIP3* virus. The AMs were co-cultured with human primary fibroblasts for indicated time. The activation of fibroblasts was evaluated by expressions of Col1 (G) and α-SMA (H), fibroblast contractility in three-dimensional collagen matrices (I), and fibroblast proliferation (J). The different colors represent different time points; the diameter indicates the relative cell viability. Scale bars, 10 μm.

Statistical significance between two groups was determined using unpaired two-tailed Student's t test; statistical significance among groups was determined using one-way ANOVA. Data are from one experiment representative of two independent experiments (A–D; mean and SEM, n = 3–5) or from three independent experiments (E–J; mean and SEM). *p < 0.05, **p < 0.01, and ***p < 0.001.

PF patients reduced the protein abundance of C/EBPβ (Figure S2C) but had no effect on *Cebpb* mRNA expression (Figure S2D). In addition, mRNA expression of *Cebpb* in AMs was comparable between PF patients and controls (Figure S2E). Indeed, A20 colocalized with C/EBPβ in AMs from PF patients (Figure S2F). Consistently, C/EBPβ expression was increased in AMs from mBLM mice (Figures S2G and S2H) and was negatively correlated with lung function (Figure S2I). Notably, expression of both C/EBPβ and Col1 increased with an increasing number of BLM exposures (Figure S2J). In addition, the mRNA expression of *Cebpb* in AMs was also comparable between mBLM- and mPBS-exposed mice (Figure S2K). Similarly, a direct interaction between A20 and C/EBPβ was observed in AMs from mBLM mouse lungs and in HEK293T cells (Figures S2L and S2M). The overexpression of A20 inhibited the expression of C/EBPβ target genes in these AMs (Figure 4D). The *in vivo* overexpression of C/EBPβ enhanced collagen deposition (Figures 4E–4G) but reduced lung function in mBLM-challenged *Tnfaip3*$^{+/-}$*Lyz2-cre* mice (Figure 4H). Notably, K63-linked ubiquitination of C/EBPβ was enhanced in AMs of fibrotic mice (Figure 4I), but A20 overexpression reduced K63-linked ubiquitination of C/EBPβ in control AMs (Figure 4J), suggesting that

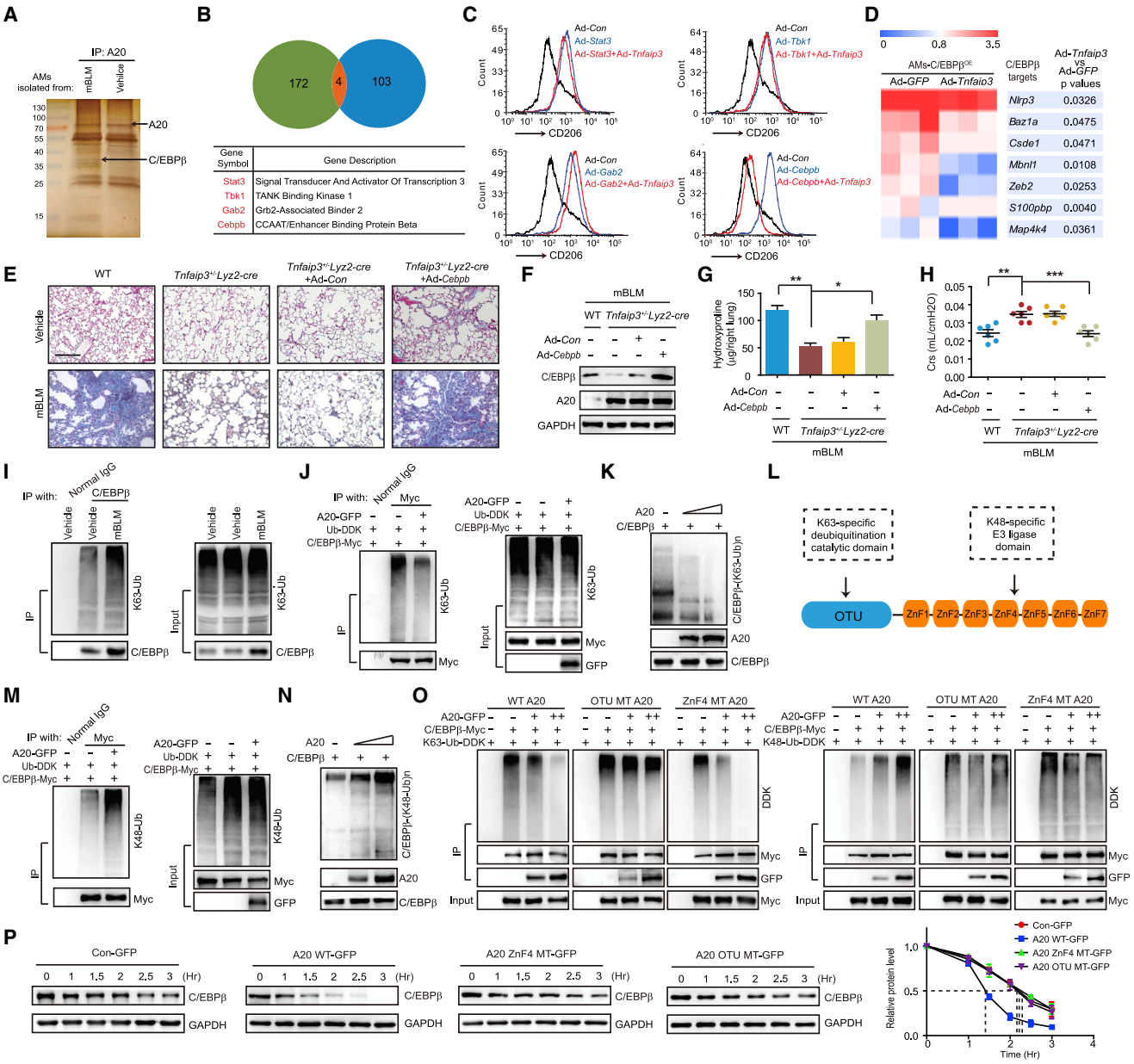

Figure 4. A20 Inhibits Profibrotic AMs by Enhancing C/EBPβ Degradation

(A) A20 protein was precipitated from the mBLM-challenged AMs. The immunocomplex was resolved by SDS-PAGE and silver staining; the bands were retrieved and analyzed by mass spectrometry (MS) analysis.

(B) Venn diagram of proteins interacting with A20 identified by MS analysis and proteins regulating AM activation reported in the literature. The red color indicates overlapping genes.

(C) Flow cytometry analyses of CD206 expression in AMs after infection with the indicated adenovirus.

(D) Gene expression profiles by RNA-seq showed that A20 expression suppressed the C/EBPβ gene signature in C/EBPβ-overexpressed AMs. The color scale indicates the $\log_2$ ratio of the normalized RNA-seq value intensities.

(E–H) Masson staining (E), A20 expression in AMs (F), hydroxyproline content in right lung (G), and Crs (H) were analyzed to evaluate the effects of C/EBPβ overexpression on the fibrotic changes in WT and *Tnfaip3*$^{+/-}$*Lyz2-cre* mice after mBLM exposure. Scale bars, 200 μm.

(I) IP assay analyzing the K63-linked ubiquitination of C/EBPβ in lung tissues from mice at day 10 after mBLM challenge.

(J) IP assay analyzing the K63-linked ubiquitination of C/EBPβ in AMs after A20 overexpression.

(K) Sample immunoblots showing the K63-linked ubiquitination of C/EBPβ in the presence of A20 *in vitro*.

(L) The domain structure of A20.

(M) IP analysis of the K48-linked ubiquitination of C/EBPβ in A20-overexpressed AMs.

(N) Sample immunoblots showing the K48-linked ubiquitination of C/EBPβ in the presence of A20 *in vitro*.

(O) Functional interplay of the OTU and ZnF4 domains of A20 in HEK293T cells. The deubiquitination of the K63-linked chains of C/EBPβ by the OTU domain of A20 is a prerequisite for C/EBPβ polyubiquitination with K48-linked chains by A20 ZnF4.

(legend continued on next page)

C/EBPβ is a substrate of A20. Recombinant A20 decreased the K63-linked ubiquitination of C/EBPβ in a concentration-dependent manner (Figure 4K), suggesting that A20 directly cleaves the K63-linked ubiquitin from C/EBPβ. The N-terminal ovarian tumor (OTU) domain is responsible for the K63-specific deubiquitination effect of A20, and zinc finger 4 (ZnF4) in the C-terminal zinc finger (ZnFs) domain mediates the K48-specific E3 ligase activity of A20 (Figure 4L) (Wertz et al., 2004). The overexpression of A20 also increased the K48-linked ubiquitination of C/EBPβ in AMs from controls (Figure 4M). Recombinant A20 enhanced the K48-linked ubiquitination of C/EBPβ in a concentration-dependent manner *in vitro* (Figure 4N). The K48-specific effect of A20 was dependent on K63 deubiquitination (Figure 4O). Thus, only overexpression of WT A20 but not the ZnF4 domain mutant or the OTU domain MT decreased C/EBPβ stability (Figure 4P). These data indicate that A20 reduces PF development by destabilizing C/EBPβ in AMs.

GSK-3β Interacts with and Phosphorylates A20 to Impede Its Function

Recent studies indicate that A20 phosphorylation regulates its deubiquitination (Hutti et al., 2007; Wertz et al., 2015). We examined A20 phosphorylation in AMs from PF patients. Higher A20 phosphorylation was found in AMs from PF patients than in AMs from controls (Figure 5A). To determine which kinase was responsible for A20 phosphorylation in AMs, the A20 immunocomplex was subjected to mass spectrometric analysis. The results showed that seven kinases could interact with A20 (Figure 5B). Among the seven kinases, *GSK3B* and *NEK7* expression was enhanced in AMs from PF patients compared with AMs from controls (Figure 5C). The overexpression of *NEK7* had no effect on A20 phosphorylation (Figure 5D), but the overexpression of GSK-3β increased A20 phosphorylation, especially threonine phosphorylation (Figure 5E). Moreover, silencing GSK-3β expression reduced the threonine phosphorylation of A20 (Figure 5F). In contrast, an *in vitro* phosphorylation assay showed that recombinant GSK-3β readily caused A20 phosphorylation in a dose-dependent manner, suggesting that A20 is a phosphorylation substrate of GSK-3β (Figure 5G). Given that A20 phosphorylation was increased in AMs from PF patients, we examined GSK-3β expression in AMs. As expected, higher GSK-3β expression was found in AMs from PF patients than in those from controls (Figures 5H and 5I). In addition, the activity of GSK-3β in PF AMs was enhanced, as indicated by the *in vitro* phosphorylated tau (Figure 5J). Consistently, the phosphorylated A20 was increased in AMs from mBLM mice (Figure S3A). Additionally, only the expression of *Gsk3b* and *Nek7* was increased in AMs from mBLM-injured mice compared with AMs from control mice (Figure S3B). Similarly, GSK-3β expression was increased in AMs from mBLM-exposed mice compared with AMs from control mice (Figures 5K and 5L). As A20 activity was suppressed in AMs from fibrotic lung tissues, we examined whether GSK-3β repressed A20 activity. Recombinant GSK-3β largely attenuated the deubiquitinating enzyme (DUB) activity of A20 *in vitro* (Figure 5M). Moreover, overexpression of GSK-3β restored not only the A20-reduced K63-linked ubiquitination of C/EBPβ (Figure 5N) but also the A20-reduced CD206 in AMs from fibrotic lung tissues (Figure 5O). The pharmacologic inhibition of GSK-3β activity reduced the expression of CD206 and C/EBPβ in AMs from mBLM mice (Figures S3C and S3D). The overexpression of GSK-3β in *Tnfaip3*$^{+/-}$*Lyz2-cre* mice enhanced collagen deposition (Figure S3E), reduced lung function (Figure S3F), and increased CD206 expression (Figure S3G) in AMs. These data indicate that GSK-3β phosphorylates A20 and suppresses its enzymatic activity in AMs.

To identify the phosphorylation sites of A20 by GSK-3β, immunoprecipitates of A20 were analyzed with mass spectrometry. A20 T454 was phosphorylated when A20 was cotransfected with GSK-3β (Figure S3H). A20 T454 is a highly conserved site across species (Figure S3I). An A20 T454A mutation reduced A20 phosphorylation (Figure S3J). Moreover, GSK-3β overexpression had no effect on the K63-linked or K48-linked ubiquitination of C/EBPβ in the presence of A20 T454A compared with WT A20 (Figures S3K and S3L). These data indicate that GSK-3β phosphorylates A20 at T454 to suppress A20 activity.

Given that A20 is a substrate of GSK-3β, a protein-protein interaction (PPI) might exist between the two proteins. Indeed, exogenous GSK-3β interacted with A20 in HEK293T cells (Figure S4A), and endogenous GSK-3β was immunoprecipitated with A20 in AMs (Figure S4B), which was confirmed by the colocalization of GSK-3β and A20 in primary mouse and human AMs (Figure S4C) and by glutathione-S-transferase (GST) pull-down assays (Figure S4D). These data indicate that GSK-3β physically interacted with A20. To map the interaction region of GSK-3β and A20, co-immunoprecipitation (coIP) assays were carried out using serial deletion mutants of either Myc-tagged A20 or HA-tagged GSK-3β. GSK-3β interacted with the OTU domain but not with the ZnFs domain of A20 (Figure S4E). Conversely, A20 interacted with the M1 domain of GSK-3β (Figure S4F). These data indicate that the OTU domain of A20 and the M1 domain of GSK-3β are required for the interaction between GSK-3β and A20.

Targeting C/EBPβ Degradation Reduces PF

Because the GSK-3β and A20 interaction enhanced the activity of the transcription factor C/EBPβ in AMs, which upregulated several profibrotic factors promoting PF development, disturbing this interaction might be a promising therapeutic strategy for PF. A number of studies have indicated that the α-helix peptides, with sequences belonging to recognition domains involved in PPIs, can be lead compounds with good druggability. We therefore screened the OTU domain of A20 with the I-TASSER server to predict the A20 secondary structure. Four α-helix structures were found in the GSK-3β-binding domain (Figure 6A). The 4 α-helices were synthesized with N-terminal and C-terminal protective amino acids, and their ability to bind with GSK-3β was measured. Peptide A displayed a high affinity for GSK-3β (K_D = 1.26 ± 2.1 nM) (Figure 6B), but there was no interaction

(P) Quantitative analyses of C/EBPβ degradation in the presence of WT A20, OUT MT A20, or ZnF4 MT A20. GAPDH was used as a loading control.
Statistical significance among groups was determined using one-way ANOVA. Data are representative of three independent experiments (C, D, I–K, and M–P; mean and SEM) or from one experiment representative of two independent experiments (E–H; mean and SEM, n = 6). *p < 0.05, **p < 0.01, and ***p < 0.001. See also Figure S3.

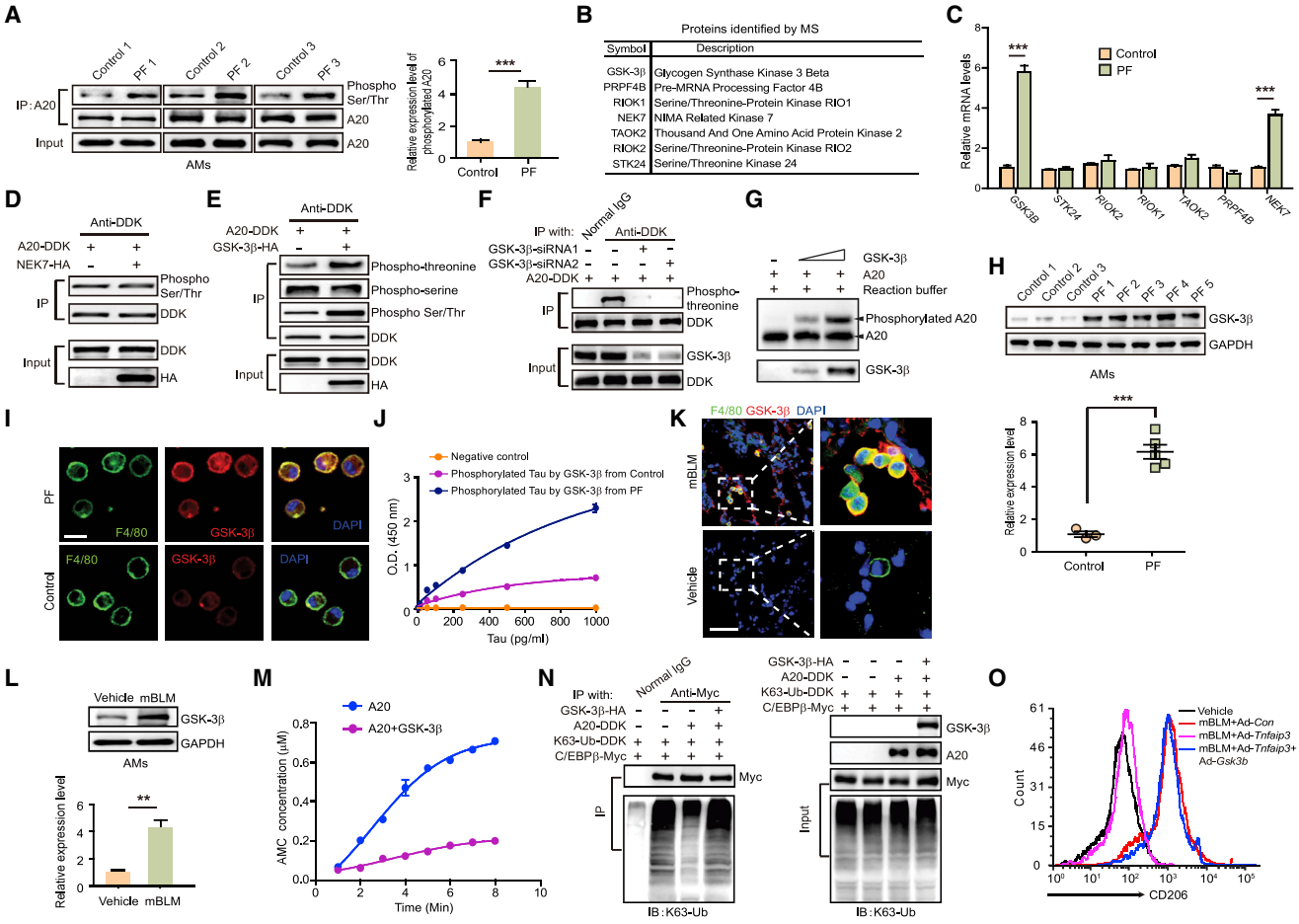

Figure 5. GSK-3β-Induced A20 Phosphorylation Interferes with A20 Enzymatic Function in AMs

(A) IP assay analyzing phosphorylated A20 in AMs from controls or PF patients.

(B) Protein kinases interacting with A20 were identified by MS.

(C) RT-PCR analyses of mRNA of A20 related kinases in AMs from controls or PF patients.

(D) IP assay analyzing phosphorylated A20 in *NEK7*-overexpressed cells.

(E) IP assay analyzing phospho-threonine and phospho-serine of A20 in GSK-3β-overexpressed cells.

(F) IP assay analyzing phosphorylated A20 in GSK-3β knockdown cells.

(G) *In vitro* phosphorylation of A20. A20 was incubated with GSK-3β in a kinase reaction buffer. Protein mixtures were separated on SDS-PAGE with Phos-tag reagent, and the phosphorylated A20 was detected with anti-A20 antibody.

(H) Quantitation of GSK-3β expression in AMs from controls (n = 3) or PF patients (n = 5). GAPDH was used as a loading control.

(I) Sample confocal images showing GSK-3β expression in AMs from controls or PF patients. Scale bars, 20 μm.

(J) GSK-3β kinase activity in AMs from controls or PF patients was determined using the Human Tau (Phospho) [pS396] ELISA Kit.

(K) Confocal images showing expressions of F4/80 and GSK-3β in lung tissues from mBLM mice. Scale bars, 50 μm.

(L) Quantitative analyses of GSK-3β expression in AMs from mouse lung at day 10 after mBLM injury. GAPDH was used as a loading control.

(M) A20 activity was measured in the presence of GSK-3β.

(N) IP analyzing deubiquitination of K63-linked chains on C/EBPβ by A20 in the presence of GSK-3β.

(O) Flow cytometry analyses of CD206 expression in AMs after treatment with the indicated adenovirus.

Statistical significance between the two groups was determined using unpaired two-tailed Student's t test. Data are representative of three independent experiments (A, C–G, N, and O; mean and SEM, n = 5 or 6) or from one experiment representative of at least two independent experiments (K–M; mean and SEM, n = 5 or 6). *p < 0.05, **p < 0.01, and ***p < 0.001. See also Figure S4.

between the other α-helices and GSK-3β (Figure S5A). To determine whether peptide A recovered A20 activity by disturbing the GSK-3β and A20 interaction, a PA fusion peptide was designed by linking a cell-penetrating peptide, Pep2, to peptide A (Li et al., 2014). A control peptide, Pcon, was generated by linking Pep2 to peptide B. PA could penetrate AMs (Figure S5B). However, only PA impeded the A20 and GSK-3β interaction (Figure 6C), accelerated C/EBPβ degradation (Figure S5C), reduced the K63-linked ubiquitination (Figure S5D), but enhanced the K48-linked ubiquitination (Figure S5E) of C/EBPβ in AMs. Moreover, PA reduced the expressions of C/EBPβ (Figure 6D) and several genes associated with the profibrotic phenotype of AMs (Figures 6E–6H) in AMs from PF patients. Thus, PA protected against the activation, proliferation, and contraction of primary human lung

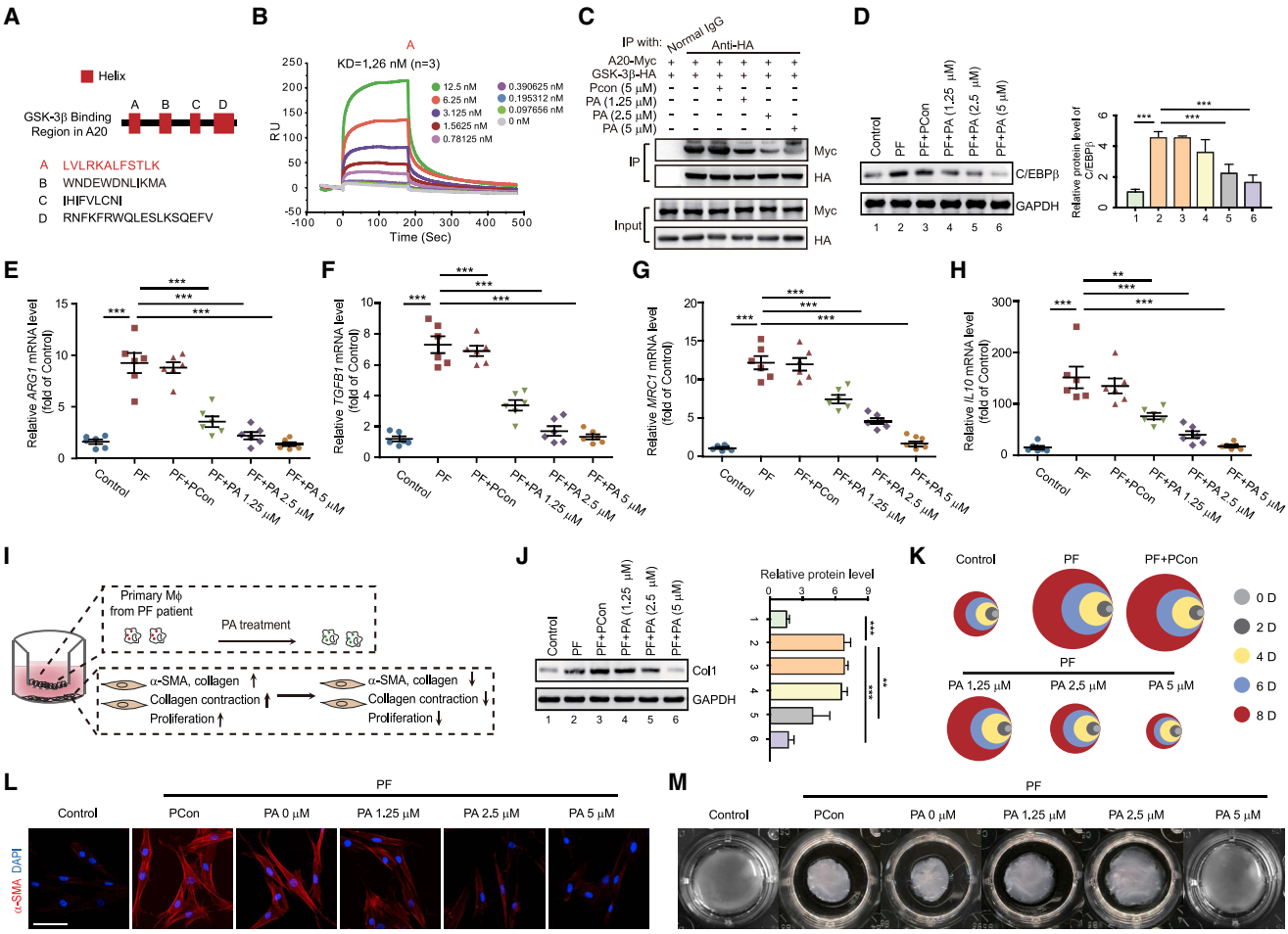

Figure 6. Disturbing the GSK-3β and A20 Interaction Recovers A20 Activity

(A) I-TASSER server analyses of the secondary structure of the GSK-3β binding region in A20 and the amino-acid sequences of the indicated α-helical peptides in A20.

(B) SPR analyses of the kinetic interaction of GSK-3β and α-helical peptides A.

(C) IP assay analyzing the A20 and GSK-3β interaction in the presence of PA.

(D) Quantitative analyses of C/EBPβ expression in AMs after PA treatment. GAPDH was used as a loading control for IB.

(E–H) mRNA amounts of *ARG1* (E), *TGFB1* (F), *MRC1* (G), and *IL10* (H) in AMs from PF patients were detected by RT-PCR after indicated treatments.

(I) The experimental scheme for detecting the communication of AMs from PF patients and primary lung fibroblasts.

(J–M) The anti-fibrotic effects of PA were evaluated by the expression of Col1 (J), fibroblast proliferation (K), α-SMA expression in fibroblasts (L), and fibroblast contractility in three-dimensional collagen matrices (M). Scale bars, 50 μm.

Statistical significance among groups was determined using one-way ANOVA. Data are representative of three independent experiments (B–D and J–M; mean and SEM) or from one experiment representative of at least two independent experiments (E–H; mean and SEM, n = 6). *p < 0.05, **p < 0.01, and ***p < 0.001. See also Figure S5.

fibroblasts caused by the culture supernatant from the profibrotic macrophages (Figures 6I–6M). In addition, disrupting the GSK3β and A20 interaction by PA suppressed the NFκB activity in AMs isolated from fibrotic mice (Figure S5F). Thus, these data verify that the GSK-3β and A20 interaction determines the profibrotic phenotype of AMs and activates myofibroblasts by enhancing the C/EBPβ stability.

We examined whether the GSK-3β-A20-C/EBPβ axis exists in monocytes, dendritic cells (DCs) or neutrophils. We first isolated both the classical and patrolling monocytes by flow cytometry analyses and detected the expression of these proteins (Figure S5G). The patrolling monocytes showed very low amounts of both A20 and C/EBPβ, while the classical monocytes expressed all these three proteins (Figure S5H). However, we did not observe an interaction between GSK-3β and A20 by coIP assay (Figure S5I). Then, DCs in lungs were isolated from PBS- and mBLM-exposed mice (Figure S5J). We found that GSK-3β protein was not expressed in DCs (Figure S5K). Although the expression of C/EBPβ was increased in DCs after BLM exposure, PA did not alter the C/EBPβ expression (Figure S5L). We examined the expressions of GSK-3β, A20, and C/EBPβ in isolated neutrophils (Figure S5M), but GSK-3β and A20 were expressed at comparable amounts in neutrophils from fibrotic and sham mouse lungs (Figure S5N). Importantly, GSK-3β could interact with A20 in these cells (Figure S5O). However, C/EBPβ in neutrophils was very low even after BLM challenge (Figure S5N).

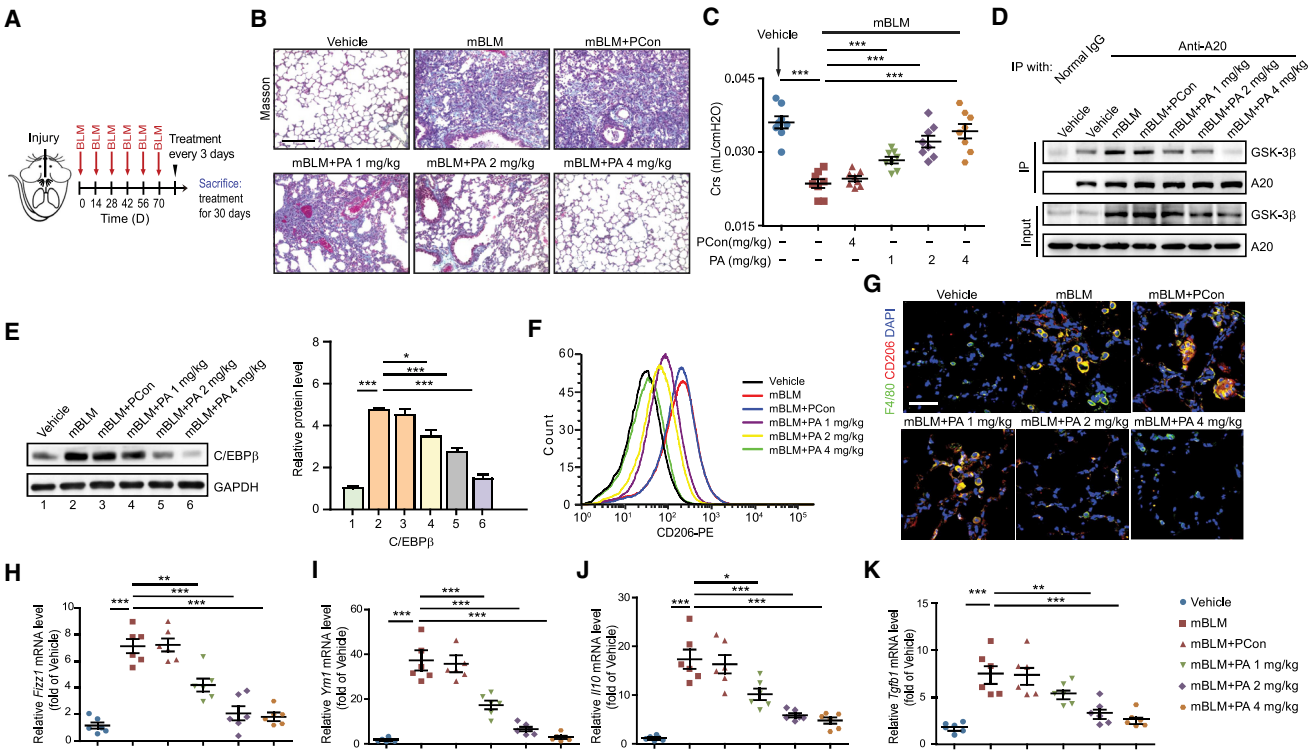

Figure 7. Disturbing the GSK-3β and A20 Interaction Reduces PF Development

(A) Schematic diagram for evaluating the therapeutic effects of PA in PF model. The mice were sacrificed by excessive anesthesia at day 40 after the last BLM challenge.

(B and C) Masson staining (B) and Crs (C) were performed to evaluate the PF changes. Scale bars, 200 μm.

(D) Sample immunoblot shows PA disturbing the interaction of A20 and GSK-3β in primary AMs.

(E) Quantitative analyses of C/EBPβ in AMs.

(F) Flow cytometry analyses of CD206 expression in PA-treated AMs.

(G) Confocal images showing the expression of F4/80 and CD206 in fibrotic lung tissues. Scale bars, 50 μm.

(H–K) Quantitative analyses of mRNA of *Fizz1* (H), *Ym1* (I), *Il10* (J), and *Tgfb1* (K) in AMs from mBLM-challenged mice treated with PA.

Statistical significance among groups was determined by one-way ANOVA. Data are from one experiment representative of at least two independent experiments (B, C, and H–K; mean and SEM, n = 6–8) or representative of three independent experiments (B–G; mean and SEM). *p < 0.05, **p < 0.01, and ***p < 0.001. See also Figures S6 and S7.

Thus, these data indicate that the GSK-3β-A20-C/EBPβ axis does not exist in monocytes, DCs, or neutrophils.

To determine if PA could attenuate PF *in vivo*, mice were treated with PA or Pcon at day 10 after mBLM exposure (Figure 7A). PA reduced collagen deposition (Figure 7B) and improved lung function (Figure 7C). Indeed, PA disturbed the GSK-3β and A20 interaction (Figure 7D) and decreased expression of C/EBPβ (Figure 7E), CD206 (Figures 7F and 7G), and several profibrotic genes (Figures 7H–7K) in AMs from mBLM mice in a dose-dependent manner. We then examined the therapeutic effects of PA on SiO_2-induced silicosis (Figure S6A). Intratracheal instillation of SiO_2 induced numerous silicotic nodules in lungs (Figure S6B) and reduced lung function (Figure S6C), but all of these changes could be ameliorated in PA-treated SiO_2 mice in a dose-dependent manner (Figures S6B and S6C). We observed a robust reduction of the GSK-3β and A20 interaction in lung tissues from PA-treated SiO_2 mice (Figure S6D). Moreover, PA reduced expression of C/EBPβ (Figure S6E), CD206 (Figure S6F), and profibrotic genes (Figures S6G–S6J) in AMs from SiO_2 PF lung tissues. In addition, PA exhibited good safety profiles in mice (Figures S6K–S6M).

To verify that PA exerted its anti-PF effect mainly via interfering with the GSK-3β and A20 interaction in AMs, we examined the role of PA in mBLM-challenged *Tnfaip3*$^{F/+}$*Lyz2-cre* mice (Figure S7A). We found that PA treatment had no effect on collagen deposition (Figure S7B), lung hydroxyproline content (Figure S7C), or lung function (Figure S7D). We isolated profibrotic AMs from mBLM-exposed mice and injected these cells into healthy mice (Figure S7E). Repeated intratracheal instillation of these cells induced fibrotic changes in lung tissues (Figure S7F), increased hydroxyproline content (Figure S7G), and reduced lung function (Figure S7H). However, PA treatment suppressed all of these changes (Figures S7F–S7H). In addition, we isolated AMs from the PA-treated mice and transferred these cells into control mice (Figure S7I). The repeated intratracheal instillation of these cells did not induce PF changes (Figures S7J–S7L). Taken together, these data indicate that the GSK-3β and A20 interaction supports the C/EBPβ stability in AMs, which promotes PF development.

Disturbing this interaction may be a potential therapeutic option for the treatment of PF.

DISCUSSION

PF complicated with ILD, including IPF, results from the repetitive alveolar epithelial injury-induced injury-repairing response, which leads to a profibrotic microenvironment in the lung. Because of the complexity and overlap of the fibrogenic process and profibrotic factors involved in PF development, the mechanisms governing the initiation, maintenance, and progression of PF remain poorly understood (Spagnolo and Maher, 2017). Inflammation is an example that has long been recognized as a major driving force for PF development. However, potent immunosuppressive and anti-inflammatory drugs show no effect on IPF progression, because of misunderstanding of the properties, duration, and intensity of inflammation in the PF process (Yang et al., 2012). Recent studies show that Mo-AMs are causally related to PF severity following lung injury (McCubbrey et al., 2018), and genetic depletion of Mo-AMs can effectively alleviate PF progression (Misharin et al., 2017). However, how Mo-AMs promote PF development has not been elucidated. In this study, we isolated Mo-AMs from PF mice models to show that A20 enzymatic activity in these cells plays crucial roles in the direction of AM phenotypes and PF development. By using several macrophage-specific A20-enhanced and A20-deficient mice and mice with chemical depletion of AMs, we sought to eliminate the influences of other immune cells, including DCs, monocytes, neutrophils, and type 2 epithelial cells. Moreover, the intratracheal instillation of AMs with high purity from *Tnfaip3*$^{F/+}$*Lyz2-cre* mice into the mice with A20 deletion plus chemical depletion of AMs not only reversed all anti-PF changes in these mice but also induced PF changes in control mice. Indeed, the dysfunction of A20 enzymatic activity but not abundance determined the profibrotic phenotype of AMs from PF patients, which verifies the observations in AMs from PF mice.

As a widely recognized anti-inflammatory protein, A20 can negatively regulate human inflammatory diseases (Vande Walle et al., 2014; Zhou et al., 2016). Although many specific substrates have been discovered, the anti-inflammatory properties of A20 are mainly thought to occur through the inhibition of NF-κB signaling. It is undeniable that the A20-NF-κB axis controls the differentiation of macrophages following acute inflammation (Wang et al., 2017b). Also, elevated A20 expression prevents Toll-like receptor-induced inflammation in macrophages (Yuk et al., 2015). Here, we found that A20 activity but not abundance in AMs was suppressed during PF. A20 activity is controlled by posttranslational modifications such as phosphorylation (Hutti et al., 2007; Wertz et al., 2015), ubiquitination (Rodriguez et al., 2014), O-glycosylation (Shrikhande et al., 2010), proteolytic cleavage (Coornaert et al., 2008), and reversible oxidation (Kulathu et al., 2013). For instance, A20 is phosphorylated by IKKβ at S381, and this increases the cleavage of K63-linked polyubiquitin chains and ZnF4-mediated ubiquitination, which generates a feedback loop to control NF-κB signaling (Wertz et al., 2015). We found that the increased GSK-3β interacted with A20 and phosphorylated A20 at T454 to suppress its activity and interfere with the degradation of C/EBPβ in AMs, which upregulated expression of the immunosuppressive and profibrotic genes. However, expression of these genes was reduced in the *Tnfaip3*$^{+/-}$*Lyz2-cre* mice whose AMs had genetically targeted A20, as indicated by the expression profiles in the scRNA-seq analysis of AMs from mBLM-exposed WT mice. The expression profiles of AMs from PF patients showed similar changes as those in AMs from fibrotic mice. Our study suggests that GSK-3β, A20, and C/EBPβ form a regulatory axis in AMs but not in monocytes, DCs, or neutrophils to control AM phenotypes during PF development. Importantly, the activation of this axis interferes with the reparative functions of AMs after mBLM- and SiO_2-induced chronic lung injury, but disruption of this axis ameliorates it.

The transcriptional factor C/EBPβ, a member of the C/EBP family of basic region-leucine zipper (bZIP) proteins, plays a crucial role in macrophage activation (Ruffell et al., 2009). C/EBPβ is an extremely labile protein, and its amount in cells is tightly controlled by ubiquitination mediated by several E3 ubiquitin ligases. These E3 ligases, including Mdm2, decrease protein stability through K48-linked polyubiquitination of their substrates (Fu et al., 2015). However, Ye et al. (2012) reported that the E3 ligase neuregulin receptor degradation protein 1 (Nrdp1) enhances C/EBPβ via K63-mediated polyubiquitination and subsequent stabilization of this protein. Indeed, the K63-linked ubiquitination of C/EBPβ was increased in AMs from fibrotic mice. However, neither the expression nor the activity of Nrdp1 was changed in AMs from mBLM mice. Actually, we found that A20 is a ubiquitin-modifying enzyme of C/EBPβ that reduces the K63-linked ubiquitination but enhances the K48-linked ubiquitination of C/EBPβ. Moreover, the K48-specific effect of A20 on C/EBPβ depends on K63-deubiquitination. Notably, overexpression of C/EBPβ enhanced PF in the mBLM-challenged *Tnfaip3*$^{+/-}$*Lyz2-cre* mice, but the elevated immunosuppressive and profibrotic genes in the C/EBPβ- overexpressed AMs could be reversed by A20 overexpression. Thus, the ubiquitin-editing function of A20 controls the C/EBPβ-mediated profibrotic phenotype of AMs.

Though they can only slow IPF progression, nintedanib and pirfenidone are two agents approved by the FDA for IPF treatment (Richeldi et al., 2017). Nintedanib is a nonspecific inhibitor of tyrosine kinase receptors and exhibits an anti-fibrotic effect by interfering with fibroblast proliferation, migration, and differentiation (Wollin et al., 2015). Whether nintedanib has any effect on profibrotic AMs is still unknown. Previous studies reported that pirfenidone suppresses PF progression by inhibiting fibroblast growth and ECM deposition. Recently, pirfenidone is reported to suppress macrophage polarization to the M2 phenotype and indirectly inhibit the activation of fibroblasts (Toda et al., 2018). However, the molecular targets of this agent remain poorly understood. Because we had observed the critical role of the GSK-3β-A20-C/EBPβ axis in PF development, we generated an α-helix peptide that disturbs the interaction of GSK-3β and A20 and exhibits a potent therapeutic effect against PF through the restoration of A20 activity and the subsequent acceleration of C/EBPβ degradation. This specific A20-derived PPI inhibitor shifted the profibrotic phenotype of AMs to the anti-fibrotic phenotype of AMs. Indeed, this PPI inhibitor may not only avoid potential off-target effects on the protein kinase GSK-3β but also make targeting the "undruggable" transcriptional factor C/EBPβ possible. Although PA acts as a competitor for GSK-3β binding,

whether this competition is specifically directed toward A20 remains to be explored. Additionally, how this peptide binds to the GSK-3β and A20 complex needs to be elucidated.

STAR★METHODS

Detailed methods are provided in the online version of this paper and include the following:

- KEY RESOURCES TABLE
- LEAD CONTACT AND MATERIALS AVAILABILITY
- EXPERIMENTAL MODEL AND SUBJECT DETAILS
  - Animal Studies
  - Human Subjects
  - Cell Lines and Primary Cultures
- METHOD DETAILS
  - Generation of Tnfaip3 genetically targeted Mice
  - Animal Model
  - Isolation of Primary Mouse Lung Fibroblasts
  - Immunoprecipitation and GST Pull-down
  - Immunoblotting and Immunostaining
  - Single-cell RNA-seq
  - Single-cell RNA-seq data preprocessing
  - Lung Function Measurement
  - Measurement of A20 Activity
  - Measurement of GSK-3β Activity
  - *In Vitro* Ubiquitination Assay
  - *In Vitro* Deubiquitination Assay
  - Silver Staining and Mass Spectrometry Analysis
  - RNA extraction and real-time PCR
  - Measurement of Hydroxyproline Amount
  - Analysis of Cellular Uptake of Peptides
  - RNA Interference
  - Analysis of Surface Plasmon Resonance
  - Plasmid Construction
  - Macrophage Transfusion
  - Three-dimensional Collagen Gels
  - Cycloheximide Treatment
  - RNA Sequencing and Analysis
  - *In Vitro* Phosphorylation Assay
  - Flow Cytometry Analysis
- QUANTIFICATION AND STATISTICAL ANALYSIS
- DATA AND CODE AVAILABILITY

SUPPLEMENTAL INFORMATION

Supplemental Information can be found online at https://doi.org/10.1016/j.immuni.2019.06.014.

ACKNOWLEDGMENTS

This work was supported by grants from the National Key R&D Program of China (2017YFA0205400), the National Natural Science Foundation of China (81530093 and 81773781 to Z.-W.H., 81803604 to S.-S.L., 81503128 to X.-X.L., and 81622010 and 81770800 to P.-P.L.), the Chinese Academy of Medical Sciences (CAMS) Central Public-Interest Scientific Institution Basal Research Fund (2017PT31046, Molecular Mechanism and Target Discovery of Metabolic Disorder and Tumorigenesis, CAMS Key Lab), and the CAMS Innovation Fund for Medical Sciences (2016-I2M-1-007 to Z.-W.H., F.H., C.-X.Z., and B.H.; 2016-I2M-1-008 to X.-X.L.; 2016-I2M-1-010 to X.-W.Z.; 2016-I2M-3-008 to B.C., J.-J.Y., S.-S.L., J.-M.Y., and X.-Y.H.; 2016-I2M-1-011 to K.L.; and 2016-I2M-4-001 to P.-P.L.).

AUTHOR CONTRIBUTIONS

Conceptualization, S.-S.L., X.-X.L., and Z.-W.H.; Methodology, C.L., J.Q., Y.-X.L., X.-P.W., F.W., S.S., C.-X.Z., and X.-Y.H.; Investigation, F.H., B.C., X.-W.Z., K.L., J.-J.Y., and J.-M.Y.; Writing – Original Draft, S.-S.L. and X.-X.L.; Writing – Review & Editing, Z.-W.H.; Resources, Z.-G.Y.; Visualization, X.L., P.-P.L., and B.H.; Funding Acquisition, S.-S.L. and Z.-W.H.; Supervision, Z.-W.H.

DECLARATION OF INTERESTS

The authors declare no competing interests.

Received: August 13, 2018
Revised: April 12, 2019
Accepted: June 18, 2019
Published: August 27, 2019

REFERENCES

Cao, Z., Lis, R., Ginsberg, M., Chavez, D., Shido, K., Rabbany, S.Y., Fong, G.H., Sakmar, T.P., Rafii, S., and Ding, B.S. (2016). Targeting of the pulmonary capillary vascular niche promotes lung alveolar repair and ameliorates fibrosis. Nat. Med. *22*, 154–162.

Coornaert, B., Baens, M., Heyninck, K., Bekaert, T., Haegman, M., Staal, J., Sun, L., Chen, Z.J., Marynen, P., and Beyaert, R. (2008). T cell antigen receptor stimulation induces MALT1 paracaspase-mediated cleavage of the NF-kappaB inhibitor A20. Nat. Immunol. *9*, 263–271.

Fu, D., Lala-Tabbert, N., Lee, H., and Wiper-Bergeron, N. (2015). Mdm2 promotes myogenesis through the ubiquitination and degradation of CCAAT/enhancer-binding protein β. J. Biol. Chem. *290*, 10200–10207.

Gordon, S. (2003). Alternative activation of macrophages. Nat. Rev. Immunol. *3*, 23–35.

He, C., Ryan, A.J., Murthy, S., and Carter, A.B. (2013). Accelerated development of pulmonary fibrosis via Cu,Zn-superoxide dismutase-induced alternative activation of macrophages. J. Biol. Chem. *288*, 20745–20757.

Hua, F., Li, K., Yu, J.J., Lv, X.X., Yan, J., Zhang, X.W., Sun, W., Lin, H., Shang, S., Wang, F., et al. (2015). TRB3 links insulin/IGF to tumour promotion by interacting with p62 and impeding autophagic/proteasomal degradations. Nat. Commun. *6*, 7951.

Huang, H., Tang, Q.Z., Wang, A.B., Chen, M., Yan, L., Liu, C., Jiang, H., Yang, Q., Bian, Z.Y., Bai, X., et al. (2010). Tumor suppressor A20 protects against cardiac hypertrophy and fibrosis by blocking transforming growth factor-beta-activated kinase 1-dependent signaling. Hypertension *56*, 232–239.

Hutti, J.E., Turk, B.E., Asara, J.M., Ma, A., Cantley, L.C., and Abbott, D.W. (2007). IkappaB kinase beta phosphorylates the K63 deubiquitinase A20 to cause feedback inhibition of the NF-kappaB pathway. Mol. Cell. Biol. *27*, 7451–7461.

Jung, S.M., Lee, J.H., Park, J., Oh, Y.S., Lee, S.K., Park, J.S., Lee, Y.S., Kim, J.H., Lee, J.Y., Bae, Y.S., et al. (2013). Smad6 inhibits non-canonical TGF-β1 signalling by recruiting the deubiquitinase A20 to TRAF6. Nat. Commun. *4*, 2562.

Kilkenny, C., Browne, W., Cuthill, I.C., Emerson, M., Altman, D.G., and Group, N.C.; NC3Rs Reporting Guidelines Working Group (2010). Animal research: reporting in vivo experiments: the ARRIVE guidelines. Br. J. Pharmacol. *160*, 1577–1579.

Kulathu, Y., Garcia, F.J., Mevissen, T.E., Busch, M., Arnaudo, N., Carroll, K.S., Barford, D., and Komander, D. (2013). Regulation of A20 and other OTU deubiquitinases by reversible oxidation. Nat. Commun. *4*, 1569.

Larson-Casey, J.L., Deshane, J.S., Ryan, A.J., Thannickal, V.J., and Carter, A.B. (2016). Macrophage Akt1 kinase-mediated mitophagy modulates apoptosis resistance and pulmonary fibrosis. Immunity *44*, 582–596.

Lee, S.H., Lee, E.J., Lee, S.Y., Kim, J.H., Shim, J.J., Shin, C., In, K.H., Kang, K.H., Uhm, C.S., Kim, H.K., et al. (2014). The effect of adipose stem cell therapy on pulmonary fibrosis induced by repetitive intratracheal bleomycin in mice. Exp. Lung Res. *40*, 117–125.

Li, K., Lv, X.X., Hua, F., Lin, H., Sun, W., Cao, W.B., Fu, X.M., Xie, J., Yu, J.J., Li, Z., et al. (2014). Targeting acute myeloid leukemia with a proapoptotic peptide conjugated to a Toll-like receptor 2-mediated cell-penetrating peptide. Int. J. Cancer *134*, 692–702.

Lv, X.X., Wang, X.X., Li, K., Wang, Z.Y., Li, Z., Lv, Q., Fu, X.M., and Hu, Z.W. (2013). Rupatadine protects against pulmonary fibrosis by attenuating PAF-mediated senescence in rodents. PLoS ONE *8*, e68631.

Ma, A., and Malynn, B.A. (2012). A20: linking a complex regulator of ubiquitylation to immunity and human disease. Nat. Rev. Immunol. *12*, 774–785.

Macosko, E.Z., Basu, A., Satija, R., Nemesh, J., Shekhar, K., Goldman, M., Tirosh, I., Bialas, A.R., Kamitaki, N., Martersteck, E.M., et al. (2015). Highly parallel genome-wide expression profiling of individual cells using nanoliter droplets. Cell *161*, 1202–1214.

Maelfait, J., Roose, K., Vereecke, L., Mc Guire, C., Sze, M., Schuijs, M.J., Willart, M., Ibañez, L.I., Hammad, H., Lambrecht, B.N., et al. (2016). A20 deficiency in lung epithelial cells protects against influenza A virus infection. PLoS Pathog. *12*, e1005410.

Malcomson, B., Wilson, H., Veglia, E., Thillaiyampalam, G., Barsden, R., Donegan, S., El Banna, A., Elborn, J.S., Ennis, M., Kelly, C., et al. (2016). Connectivity mapping (ssCMap) to predict A20-inducing drugs and their anti-inflammatory action in cystic fibrosis. Proc. Natl. Acad. Sci. U S A *113*, E3725–E3734.

McCubbrey, A.L., Barthel, L., Mohning, M.P., Redente, E.F., Mould, K.J., Thomas, S.M., Leach, S.M., Danhorn, T., Gibbings, S.L., Jakubzick, C.V., et al. (2018). Deletion of c-FLIP from CD11b^{hi} macrophages prevents development of bleomycin-induced lung fibrosis. Am. J. Respir. Cell Mol. Biol. *58*, 66–78.

McQuattie-Pimentel, A.C., Budinger, G.R.S., and Ballinger, M.N. (2018). Monocyte-derived alveolar macrophages: the dark side of lung repair? Am. J. Respir. Cell Mol. Biol. *58*, 5–6.

Misharin, A.V., Morales-Nebreda, L., Reyfman, P.A., Cuda, C.M., Walter, J.M., McQuattie-Pimentel, A.C., Chen, C.I., Anekalla, K.R., Joshi, N., Williams, K.J.N., et al. (2017). Monocyte-derived alveolar macrophages drive lung fibrosis and persist in the lung over the life span. J. Exp. Med. *214*, 2387–2404.

Mora, A.L., Torres-González, E., Rojas, M., Corredor, C., Ritzenthaler, J., Xu, J., Roman, J., Brigham, K., and Stecenko, A. (2006). Activation of alveolar macrophages via the alternative pathway in herpesvirus-induced lung fibrosis. Am. J. Respir. Cell Mol. Biol. *35*, 466–473.

Nair, M.G., Du, Y., Perrigoue, J.G., Zaph, C., Taylor, J.J., Goldschmidt, M., Swain, G.P., Yancopoulos, G.D., Valenzuela, D.M., Murphy, A., et al. (2009). Alternatively activated macrophage-derived RELM-alpha is a negative regulator of type 2 inflammation in the lung. J. Exp. Med. *206*, 937–952.

Osborn-Heaford, H.L., Murthy, S., Gu, L., Larson-Casey, J.L., Ryan, A.J., Shi, L., Glogauer, M., Neighbors, J.D., Hohl, R., and Carter, A.B. (2015). Targeting the isoprenoid pathway to abrogate progression of pulmonary fibrosis. Free Radic. Biol. Med. *86*, 47–56.

Pardo, A., and Selman, M. (2016). Lung fibroblasts, aging, and idiopathic pulmonary fibrosis. Ann. Am. Thorac. Soc. *13* (*Suppl 5*), S417–S421.

Putman, R.K., Hatabu, H., Araki, T., Gudmundsson, G., Gao, W., Nishino, M., Okajima, Y., Dupuis, J., Latourelle, J.C., Cho, M.H., et al.; Evaluation of COPD Longitudinally to Identify Predictive Surrogate Endpoints (ECLIPSE) Investigators; COPDGene Investigators (2016). Association between interstitial lung abnormalities and all-cause mortality. JAMA *315*, 672–681.

Redente, E.F., Keith, R.C., Janssen, W., Henson, P.M., Ortiz, L.A., Downey, G.P., Bratton, D.L., and Riches, D.W. (2014). Tumor necrosis factor-α accelerates the resolution of established pulmonary fibrosis in mice by targeting profibrotic lung macrophages. Am. J. Respir. Cell Mol. Biol. *50*, 825–837.

Richeldi, L., Collard, H.R., and Jones, M.G. (2017). Idiopathic pulmonary fibrosis. Lancet *389*, 1941–1952.

Rodriguez, M.S., Egaña, I., Lopitz-Otsoa, F., Aillet, F., Lopez-Mato, M.P., Dorronsoro, A., Lobato-Gil, S., Sutherland, J.D., Barrio, R., Trigueros, C., and Lang, V. (2014). The RING ubiquitin E3 RNF114 interacts with A20 and modulates NF-κB activity and T-cell activation. Cell Death Dis. *5*, e1399.

Ruffell, D., Mourkioti, F., Gambardella, A., Kirstetter, P., Lopez, R.G., Rosenthal, N., and Nerlov, C. (2009). A CREB-C/EBPbeta cascade induces M2 macrophage-specific gene expression and promotes muscle injury repair. Proc. Natl. Acad. Sci. U S A *106*, 17475–17480.

Schuijs, M.J., Willart, M.A., Vergote, K., Gras, D., Deswarte, K., Ege, M.J., Madeira, F.B., Beyaert, R., van Loo, G., Bracher, F., et al. (2015). Farm dust and endotoxin protect against allergy through A20 induction in lung epithelial cells. Science *349*, 1106–1110.

Shrikhande, G.V., Scali, S.T., da Silva, C.G., Damrauer, S.M., Csizmadia, E., Putheti, P., Matthey, M., Arjoon, R., Patel, R., Siracuse, J.J., et al. (2010). O-glycosylation regulates ubiquitination and degradation of the anti-inflammatory protein A20 to accelerate atherosclerosis in diabetic ApoE-null mice. PLoS ONE *5*, e14240.

Spagnolo, P., and Maher, T.M. (2017). Clinical trial research in focus: why do so many clinical trials fail in IPF? Lancet Respir. Med. *5*, 372–374.

Toda, M., Mizuguchi, S., Minamiyama, Y., Yamamoto-Oka, H., Aota, T., Kubo, S., Nishiyama, N., Shibata, T., and Takemura, S. (2018). Pirfenidone suppresses polarization to M2 phenotype macrophages and the fibrogenic activity of rat lung fibroblasts. J. Clin. Biochem. Nutr. *63*, 58–65.

Vande Walle, L., Van Opdenbosch, N., Jacques, P., Fossoul, A., Verheugen, E., Vogel, P., Beyaert, R., Elewaut, D., Kanneganti, T.D., van Loo, G., and Lamkanfi, M. (2014). Negative regulation of the NLRP3 inflammasome by A20 protects against arthritis. Nature *512*, 69–73.

Wang, X., Ai, L., Xu, Q., Wu, C., Chen, Z., Su, D., Jiang, X., and Fan, Z. (2017a). A20 Attenuates Liver Fibrosis in NAFLD and Inhibits Inflammation Responses. Inflammation *40*, 840–848.

Wang, Y., Song, Z., Bi, J., Liu, J., Tong, L., Song, Y., Bai, C., and Zhu, X. (2017b). A20 protein regulates lipopolysaccharide-induced acute lung injury by downregulation of NF-κB and macrophage polarization in rats. Mol. Med. Rep. *16*, 4964–4972.

Wertz, I.E., O'Rourke, K.M., Zhou, H., Eby, M., Aravind, L., Seshagiri, S., Wu, P., Wiesmann, C., Baker, R., Boone, D.L., et al. (2004). De-ubiquitination and ubiquitin ligase domains of A20 downregulate NF-kappaB signalling. Nature *430*, 694–699.

Wertz, I.E., Newton, K., Seshasayee, D., Kusam, S., Lam, C., Zhang, J., Popovych, N., Helgason, E., Schoeffler, A., Jeet, S., et al. (2015). Phosphorylation and linear ubiquitin direct A20 inhibition of inflammation. Nature *528*, 370–375.

Wollin, L., Wex, E., Pautsch, A., Schnapp, G., Hostettler, K.E., Stowasser, S., and Kolb, M. (2015). Mode of action of nintedanib in the treatment of idiopathic pulmonary fibrosis. Eur. Respir. J. *45*, 1434–1445.

Wynn, T.A., and Vannella, K.M. (2016). Macrophages in tissue repair, regeneration, and fibrosis. Immunity *44*, 450–462.

Yang, H.Z., Wang, J.P., Mi, S., Liu, H.Z., Cui, B., Yan, H.M., Yan, J., Li, Z., Liu, H., Hua, F., et al. (2012). TLR4 activity is required in the resolution of pulmonary inflammation and fibrosis after acute and chronic lung injury. Am. J. Pathol. *180*, 275–292.

Ye, S., Xu, H., Jin, J., Yang, M., Wang, C., Yu, Y., and Cao, X. (2012). The E3 ubiquitin ligase neuregulin receptor degradation protein 1 (Nrdp1) promotes M2 macrophage polarization by ubiquitinating and activating transcription factor CCAAT/enhancer-binding protein b (C/EBPb). J. Biol. Chem. *287*, 26740–26748.

Yuk, J.M., Kim, T.S., Kim, S.Y., Lee, H.M., Han, J., Dufour, C.R., Kim, J.K., Jin, H.S., Yang, C.S., Park, K.S., et al. (2015). Orphan nuclear receptor ERRα controls macrophage metabolic signaling and A20 expression to negatively regulate TLR-induced inflammation. Immunity *43*, 80–91.

Zhou, Q., Wang, H., Schwartz, D.M., Stoffels, M., Park, Y.H., Zhang, Y., Yang, D., Demirkaya, E., Takeuchi, M., Tsai, W.L., et al. (2016). Loss-of-function mutations in TNFAIP3 leading to A20 haploinsufficiency cause an early-onset autoinflammatory disease. Nat. Genet. *48*, 67–73.

STAR★METHODS

KEY RESOURCES TABLE

REAGENT or RESOURCE	SOURCE	IDENTIFIER
Antibodies		
TNFAIP3	Abcam	Cat#ab13597; RRID: AB_300491
Collagen I	Abcam	Cat#ab34710; RRID: AB_731684
C/EBPβ	Abcam	Cat#ab32358; RRID: AB_726796
F4/80	Abcam	Cat#ab6640; RRID: AB_1140040
GSK-3β (clone D5C5Z)	CST	Cat#12456s; RRID: AB_2636978
Ubiquitin	CST	Cat#3933s; RRID: AB_2180538
K63-linkage Specific Polyubiquitin (clone D7A11)	CST	Cat#5621s; RRID: AB_10827985
K48-linkage Specific Polyubiquitin (clone D9D5)	CST	Cat#8081s; RRID: AB_10859893
Anti-HA-tag	MBL BIOTECH	Cat#561; RRID: AB_591839
Anti-GFP-tag	MBL BIOTECH	Cat#598; RRID: AB_591819
Anti-DDDDK-tag	MBL BIOTECH	Cat#M185-3L; RRID: AB_11123930
α-SMA	BOSTER	Cat#BM0002; RRID: AB_2811044
Donkey anti-mouse Alexa 488	Life Technologies	Cat#A21206; RRID: AB_141708
Donkey anti-rabbit Alexa 647	Life Technologies	Cat#A31571; RRID: AB_162542
GAPDH	ZSGB BIO	Cat#TA-08; RRID: AB_2747414
Peroxidase-Conjugated Goat anti-Rabbit IgG	ZSGB BIO	Cat#ZB-2301; RRID: AB_2747412
Peroxidase-Conjugated Goat anti-Mouse IgG	ZSGB BIO	Cat#ZB-2305; RRID: AB_2747415
FITC anti-mouse CD206	Biolegend	Cat#141704; RRID: AB_2221822
PE anti-mouse F4/80	Biolegend	Cat#123109; RRID: AB_893498
FITC anti-mouse CD45 (clone 30-F11)	Biolegend	Cat # 103108; RRID: AB_312973
APC anti-mouse CD11b (clone M1/70)	Biolegend	Cat #101212; RRID: AB_312795
BV421 anti-mouse CD64 (clone X54-5/7.1)	Biolegend	Cat#139309; RRID: AB_2562694
Percp/cy5.5 anti-mouse Ly6G (clone 1A8)	Biolegend	Cat #127616; RRID: AB_1877271
Percp/cy5.5 anti-mouse Ly6C (clone HK1.4)	Biolegend	Cat #128012; RRID: AB_1659241
Bacterial and Virus Strains		
A20 overexpression adenovirus	HanBio Co., Ltd	N/A
C/EBPβ overexpression adenovirus	HanBio Co., Ltd	N/A
GSK-3β overexpression adenovirus	HanBio Co., Ltd	N/A
Stat3 overexpression adenovirus	HanBio Co., Ltd	N/A
Tbk1 overexpression adenovirus	HanBio Co., Ltd	N/A
Gab2 overexpression adenovirus	HanBio Co., Ltd	N/A
GFP adenovirus	HanBio Co., Ltd	N/A
Biological Samples		
Primary PF patient BALF samples	Pulmonary Function Detection Chamber of Friendship Hospital	http://www.bfh.com.cn/
Chemicals, Peptides, and Recombinant Proteins		
GSK-3β-GST protein	Novus Biologicals	Cat #2506-KS-010
A20 protein	Abcam	Cat #ab198780
Recombinant human Ubiquitin K48 only protein	Abcam	Cat #ab157048
BLM	Nippon Kayaku, Japan	Cat #ECS001668
Cycloheximid (CHX)	Sigma Aldrich	Cat #R750107
Peptide A, B, C, D, PA	SBS Genetech Co., Ltd	N/A
SC75741	Selleck	Cat #S7273

(*Continued on next page*)

Continued

REAGENT or RESOURCE	SOURCE	IDENTIFIER
1-Azakenpaullone	Selleck	Cat #S7193
Critical Commercial Assays		
RNA Sequencing Assay (Illunima HiSeq 4000)	KangChen Biotech Company	N/A
Human Tau [pS396] ELISA kit	Invitrogen, Carlsbad, CA	Cat #KHB7031
DUB Activity Kit	StressMarq Biosciences INC.	Cat #SKT-136
Pierce® Silver Stain for Mass Spectrometry Kit	thermo scientific	Cat #24600
Pierce Co-Immunoprecipitation Kit	thermo scientific	Cat #26149
Hydroxyproline Measurement Kit	NanJing JianCheng Bioengineering Institute	Cat #A030-2
Deposited Data		
Raw and analyzed data	This paper	SRA: SRR10007823, SRR10007824; GEO: GSE117690
Experimental Models: Cell Lines		
HEK293T cells	BIOLEAF SCIENCE	N/A
Experimental Models: Organisms/Strains		
Tnfaip3 genetically targeted Mouse	Cyagen Biosciences	N/A
B6;129P2-*Tnfaip3* < tm1Homy >	RIKEN BioResource Center	RBRC05494; RRID: IMSR_RBRC05494
B6.129P2-Lyz2tm1(cre)/Nju (LysM-Cre)	Model Animal Resource Information Platform	N000056
Oligonucleotides		
The sequences of the realtime PCR primers, see Table S2	This paper	N/A
Recombinant DNA		
A20-GFP	Genecopoeia	Cat #EX-Mm21251-M32
A20-Myc-DDK	OriGene	Cat #MR210582
C/EBPβ-Myc-DDK	OriGene	Cat #MR227563
GSK-3β-HA	Sino Biological Inc.	Cat #MG50650-NY
Nek7-HA	Genecopoeia	Cat #EX-Mm08105-M06
Control-Flag (3x FLAG System Expression Vectors)	Sigma Aldrich	Cat #E4151
Other recombinant DNA, see Star Methods text	This paper	N/A
Software and Algorithms		
Graphpad Prism 6.0 software	Graph Pad Software, Inc.	http://www.graphpad.com/scientific-software/prism/
FCS EXPRESS 6	De Novo Software, Inc	http://www.denovosoftware.com

LEAD CONTACT AND MATERIALS AVAILABILITY

Further information and requests for resources and reagents should be directed to and will be fulfilled by the Lead Contact, Zhuo-Wei Hu (huzhuowei@imm.ac.cn).

EXPERIMENTAL MODEL AND SUBJECT DETAILS

Animal Studies

C57BL/6J mice (18-20 g, 6-8 weeks old) were purchased from Vital River Lab Animal Technology Co., Ltd. (Beijing, China). A20 conditional targeted (*Tnfaip3*$^{+/-}$) mice were generated as described in Figure 1A by Cyagen Biosciences Inc. (Guangzhou, China). A20 conditional deficient (*Tnfaip3*$^{F/+}$) mice were purchased from RIKEN (Wako, Japan). *Lyz2-cre* mice and *Sftpc-cre* mice were purchased from the Model Animal Research Center of Nanjing University (Nanjing, China). *Itgax-cre* mice were purchased from SHANGHAI MODEL ORGANISMS (Shanghai, China). *Tnfaip3*$^{+/-}$*Lyz2-cre* mice and *Tnfaip3*$^{F/+}$*Lyz2-cre* mice were generated by intercrossing *Tnfaip3*$^{+/-}$ transgenic mice or *Tnfaip3*$^{F/+}$ transgenic mice with *Lyz2-cre* mice. *Tnfaip3*$^{+/-}$*Itgax-cre* mice and *Tnfaip3*$^{F/+}$*Itgax-cre* mice were generated by intercrossing *Tnfaip3*$^{+/-}$ transgenic mice or *Tnfaip3*$^{F/+}$ transgenic mice with *Itgax-cre* mice. *Tnfaip3*$^{+/-}$*Sftpc-cre* mice were generated by intercrossing *Tnfaip3*$^{+/-}$ transgenic mice with *Sftpc-cre* mice. These mice

were maintained in the animal facility at the Institute of Materia Medica under specific-pathogen-free (SPF) conditions. For animal studies, the mice were earmarked before grouping and were then randomly separated into groups by an independent person. However, no particular method of randomization was used. The sample size was predetermined empirically according to previous experience using the same strains and treatments. Generally, we used $n \geq 6$ mice per genotype and condition. We ensured that the experimental groups were balanced in terms of animal age and weight. In all experiments, young adult (6-8 weeks) male mice were used. All animal studies were approved by the Animal Experimentation Ethics Committee of the Chinese Academy of Medical Sciences (Permit No. 002802), and all procedures were conducted in accordance with the guidelines of the Institutional Animal Care and Use Committees of the Chinese Academy of Medical Sciences. All animal procedures were consistent with the ARRIVE guidelines (Kilkenny et al., 2010).

Human Subjects

We obtained human AMs from the Pulmonary Function Detection Chamber of Beijing Friendship Hospital. Primary AMs were isolated from the lungs of human subjects with IPF as previously described (Osborn-Heaford et al., 2015). The clinical features of the patients are listed in Table S1. All protocols using human specimens were approved by the Institutional Review Board of the Chinese Academy of Medical Sciences and Peking Union Medical College. Informed consent was obtained from all subjects. The study conformed to the principles outlined in the Declaration of Helsinki.

Cell Lines and Primary Cultures

Primary human lung fibroblasts (PriCells) were cultured in DMEM/F12 supplemented with 10% fetal bovine serum (FBS). The human embryonic kidney cell line HEK293T (ATCC, CRL-11268) was cultured in IMDM supplemented with 10% FBS. Primary mouse lung fibroblasts were cultured in DMEM with 15% FBS. Primary human and mouse AMs were cultured in RPMI 1640 medium with 10% FBS. All cells were cultured at 37°C under 5% CO_2 in a high-humidity atmosphere. The cells were authenticated by morphological examination and were confirmed to be mycoplasma free.

METHOD DETAILS

Generation of Tnfaip3 genetically targeted Mice

Tnfaip3 conditional genetically targeted (*Tnfaip3*$^{+/-}$) mice were generated by Cyagen Biosciences Inc. using CRISPR/Cas-mediated genome engineering. The mouse *Tnfaip3* gene (GenBank accession number: NM_009397.3) is located on mouse chromosome 10. For the genetically targeted model, the "CAG-LoxP-Stop-LoxP-mouse *Tnfaip3* cDNA-polyA" cassette was cloned into intron 1 of ROSA26. The expression of mouse *Tnfaip3* cDNA was dependent on the expression of Cre recombinase. To engineer the donor vector, homology arms were generated by PCR using a BAC clone from the C57BL/6J library as a template. Cas9 and gRNA were co-injected into fertilized eggs with the donor vector to produce genetically targeted mice. The pups were genotyped by PCR followed by sequencing of the PCR product.

Animal Model

The mouse model of irreversible PF was generated by repetitive intratracheal BLM spray as previously described, with some modifications (Cao et al., 2016; Lee et al., 2014). Briefly, mice were anesthetized with 400 mg/kg Avertin i.p. (Sigma-Aldrich). BLM (Nippon Kayaku) in 50 μL of LPS-free PBS (1 U/kg) was sprayed into the trachea using a MicroSprayer (Penn-Century) a total of 6 times, with 14 days between each spray. Mice were sacrificed by excessive anesthesia at day 40 after the 6th BLM spray. The reversible PF model was generated by single intratracheal instillation of BLM (3 U/kg) in 50 μL of LPS-free PBS, and the mice were sacrificed by excessive anesthesia at the indicated time points after exposure. The silicosis mouse model was generated by a single intratracheal dose of a 125 mg/kg silica particle suspension (Sigma-Aldrich), and the mice were sacrificed at day 50 after the SiO_2 administration. Mice in the sham groups were treated intratracheally with an identical volume of PBS. For therapeutic experiments, mice were i.p. injected with the indicated agents every 3 days beginning at day 10 after the last BLM operation or at day 50 after SiO_2 challenge for 30 days. Mice were sacrificed by excessive anesthesia 40 days after the last BLM challenge or 80 days after SiO_2 challenge.

Isolation of Primary Mouse Lung Fibroblasts

Mice were sacrificed with excessive anesthesia and cleaned with alcohol wipes. The chest was opened, and the left pulmonary lobe was sheared in sterile PBS. After being rinsed twice, the lung lobe was cut into ~1 mm^3 pieces in culture medium. The tissue was centrifuged at 600 × *g* for 10 min, and the pellet was resuspended in DMEM with 15% FBS in a 10 cm dish. The adherent cells were harvested for passage or other assays after 4-5 days of culture.

Immunoprecipitation and GST Pull-down

The treated cells were collected, centrifuged at 3000 rpm for 5 min, and lysed for 30 min on ice with constant mixing. After being centrifuged for 30 min at 12000 rpm, 10% of the soluble lysate was set aside as input, and the remainder was incubated with a specific antibody at 4°C overnight and then incubated with Protein A/G Plus–agarose (Santa Cruz) beads at 4°C for 2 hr. Then, the immunocomplexes were mixed with 5 × loading buffer and boiled for 10 min at 98°C. The precipitated proteins were subjected to SDS-PAGE and analyzed with corresponding antibodies. For the GST pull-down assay, purified A20 protein (Abcam) was

incubated with GST or a GST-C/EBPβ fusion protein (Novus Biologicals) and glutathione-Sepharose beads (GE) with rotation at 4°C overnight. After 4 washes with PBS, 30 μL of 2 × loading buffer was added to the precipitated beads. Then, the mixtures were boiled for 10 min at 98°C. The combination of proteins was confirmed by SDS-PAGE and Coomassie blue staining.

Immunoblotting and Immunostaining

Proteins were extracted from cultured cells and lung tissues with RIPA buffer (Cell Signaling Technology). BCA protein assay kits (Beyotime Technology) were used to measure the protein concentrations. Lysates were resolved with SDS-PAGE and transferred to PVDF membranes for immunoblotting. The images were captured by a LAS4000 Image Station (General Electric Company). For immunofluorescence staining, cells grown on coverslips and frozen sections of tissues were fixed with 4% paraformaldehyde, permeabilized with 0.5% Triton X-100 for 20 min, treated with 3% BSA at 37°C for 30 min, and then incubated with the indicated antibodies at 4°C overnight. After being washed 3 times in PBS, the cells were stained with the corresponding secondary antibodies (goat anti-mouse Alexa 488 (1:200) and/or goat anti-rabbit Alexa 647 (1:200)) for 2 hr at room temperature. Nuclei were visualized with 4,6-diamidino-2-phenylindole (DAPI) staining before the sections were covered with coverslips. Images were obtained with a confocal microscope (Leica Microsystems, Heidelberg, GmbH, TCS SP2).

Single-cell RNA-seq

Single-cell RNA-seq libraries were prepared with Chromium Single cell 3′ Reagent v2 Kits according to the manufacturer's protocol. Single-cell suspensions were loaded on the Chromium Single Cell Controller Instrument (10 × Genomics) to generate single cell gel beads in emulsions (GEMs). Briefly, 10^5 single cells were suspended in calcium- and magnesium-free PBS containing 0.04% weight/volume BSA. About 15000-20000 cells were added to each channel with a targeted cell recovery estimate of 10000 cells (9675 for WT mice and 12947 for *Tnfaip3*$^{+/-}$*Lyz2-cre* mice). After generation of GEMs, reverse transcription reactions were engaged barcoded full-length cDNA followed by the disruption of emulsions using the recovery agent and cDNA clean up with DynaBeads Myone Silane Beads (Thermo Fisher Scientific). cDNA was then amplified by PCR with appropriate cycles which depend on the recovery cells. Subsequently, the amplified cDNA was fragmented, end-repaired, A-tailed, index adaptor ligated and library amplification. Then these libraries were sequenced on the Illumina sequencing platform (HiSeq X Ten), and 150 bp paired-end reads were generated.

Single-cell RNA-seq data preprocessing

The Cell Ranger software pipeline (version 2.2.0) provided by 10 × Genomics was used to demultiplex cellular barcodes, map reads to the genome and transcriptome using the STAR aligner, and downsample reads as required to generate normalized aggregate data across samples, producing a matrix of gene counts versus cells. We processed the unique molecular identifier (UMI) count matrix using the R package Seurat (version 2.3.4). As a quality-control step, the gene expressed less than 1% cells were discarded. To remove low-quality cells and likely multiplet captures, which is a major concern in microdroplet-based experiments, we further apply a criteria to filter out cells with UMI/gene numbers out of the limit of mean value ± 2 fold of standard devitation, which assuming a Guassian distribution of each cells' UMI/gene numbers. Following visual inspection of the distribution of cells by the fraction of mitochondrial genes expressed, we further discarded low-quality cells where > 10% of the counts belonged to mitochondrial genes. After applying these quality control criteria, 8501 single cells and 1908 genes for WT mice and 11742 cells and 1924 genes for *Tnfaip3*$^{+/-}$*Lyz2-cre* mice remained and were included in downstream analyses. Library size normalization was performed in Seurat on the filtered matrix to obtain the normalized count.

Top variable genes across single cells were identified using the method described previously (Macosko et al., 2015). Briefly, the average expression and dispersion were calculated for each gene, genes were subsequently placed into 11 bins based on expression. Principal component analysis was performed to reduce the dimensionality on the log transformed gene-barcode matrices of top variable genes. Cells were clustered based on a graph-based clustering approach, and were visualized in 2-dimension using tSNE. Likelihood ratio test that simultaneously test for changes in mean expression and in the percentage of expressed cells was used to identify differentially expressed genes between clusters. The SRA accession numbers are in this study.

Lung Function Measurement

Mice were i.p. injected with 0.4 g/kg tribromoethanol and placed on a flexiVent pulmonary system (SCIREQ Inc.). Then, the mice were subjected to mechanical ventilation with a tidal volume of 10 ml/kg and a respiratory rate of 150 breaths/min; 3 cmH_2O positive end expiratory pressure (PEEP) was used for lung function evaluation as described previously (Lv et al., 2013). The dynamic pulmonary compliance was measured by Snapshot-150 perturbation.

Measurement of A20 Activity

Total protein was extracted from AMs in mouse or PF patient lung tissues through homogenization in RIPA buffer obtained from Beyotime Biotechnology. A20 protein was coimmunoprecipitated with the corresponding antibody (Abcam). The beads were then washed five times. The target protein (A20) was eluted with elution buffer from a Pierce Co-Immunoprecipitation Kit purchased from Thermo Scientific. The deubiquitinating enzyme (DUB) activity of A20 in AMs was measured with a DUB Activity Kit from StressMarq Biosciences Inc., according to the manufacturer's instructions. Fluorescence intensity was measured using a microplate reader, and data were analyzed based on an AMC standard curve.

Measurement of GSK-3β Activity

GSK-3β protein was immunoprecipitated from AMs of PF patients or controls. Then, the protein was added to a reaction buffer containing 40 mM HEPES (pH 7.2), 5 mM $MgCl_2$, 5 mM EDTA, 50 μg/ml heparin and 100 μM ATP with recombinant human TAU-441 (Millipore). Reaction mixtures were incubated at 30°C for 1 hr. The amount of phosphorylated TAU-441 was measured with a human Tau [pS396] ELISA kit (Invitrogen). The absorbance of each reaction at 450 nm was read by an HTS 7000 Plus Bio Assay Reader (Perkin Elmer). The GSK-3β activity curves were fit and drawn in GraphPad Prism 5 with the four-parameter algorithm.

In Vitro Ubiquitination Assay

The plasmids A20-DDK and C/EBPβ-Myc were separately transfected into HEK293T cells. The labeled A20 and C/EBPβ proteins were detected with tag antibodies via coimmunoprecipitation. Ingredients including 10 × E1 (Boston Biochem), 10 × E2 (Boston Biochem), 10 mM ATP (New England Biolabs), 10 × buffer (Boston Biochem), and Ub (Abcam) were mixed with the A20 and C/EBPβ immunoprecipitated proteins in a total reaction volume of 30 μL and incubated at 37°C for 2.5 hr. Once the 5 × loading buffer was added, the proteins were denatured at 98°C for 10 min. The mix was subjected to SDS-PAGE for the detection of ubiquitination.

In Vitro Deubiquitination Assay

Myc-C/EBPβ substrate with polyubiquitin chains was immunoprecipitated from C/EBPβ-and Ub-overexpressed 293T cells. Myc-C/EBPβ immunoprecipitates were washed four times with PBS. Low dose (0.5 mg) or high dose (1 mg) A20 protein (Abcam) and C/EBPβ substrates were combined in a buffer containing 50 mM HEPES (pH 8.0), 0.01% Brij-35 and 3 mM DTT and incubated at 37°C for 120 min. After the reaction was complete, the mixture was boiled in 5 × sample buffer, resolved by 10% SDS-PAGE and immunoblotted with an antibody against K63-Ub (Cell Signaling Technology).

Silver Staining and Mass Spectrometry Analysis

The experiment was carried out according to the manufacturer's instructions for the Pierce® Silver Stain for Mass Spectrometry Kit (Thermo Scientific). Briefly, the A20 protein and its interacting proteins were coimmunoprecipitated with the corresponding antibody, and the proteins were denatured in SDS solution and subjected to SDS-PAGE followed by silver staining. The bands were extracted from the gel and subjected to LC-MS/MS sequencing and data analysis by QLBio Biotechnology Co., Ltd. (Beijing, China). Briefly, the proteins were digested and extracted from the gel. The digestion products were separated by a 120/60 min gradient elution at a flow rate of 0.600 μl/min with an EASY-nLC 1000 system, which was directly interfaced with a Thermo Orbitrap Fusion mass spectrometer. The masses of the peptides were identified by an LC-MS/MS Q Exactive Hybrid Quadrupole-Orbitrap Mass Spectrometer (Thermo Scientific). MS/MS data were searched against the human FASTA sequences from UniProt using an in-house Proteome Discoverer (Version PD1.4, Thermo Fisher Scientific). Only peptides that were assigned to a given protein group were considered unique.

RNA extraction and real-time PCR

Total RNA from tissues or cell samples was extracted according to the manufacturer's instructions using TransZol Up reagent (TransGen). cDNA was synthesized via reverse transcription with *TransScript* RT/RI Enzyme Mix and Anchored Oligo (dT) primers (TransGen). Gene expression was analyzed via real-time PCR assay. The PCR amplification was performed in triplicate, and each reaction consisting of 1x SYBR FAST qPCR Master Mix (KAPA BIOSYSTEMS), 1 μL of mixed primers and 1 μL of template cDNA was run for 40 cycles using LineGene 9620 apparatus (Bioer). The program was set for enzyme activation (95°C, 3 min); denaturation (95°C, 3 s); and annealing extension (60°C, 20 s). The sequences of the primers are listed in Table S2. Data acquisition and the analysis of real-time PCR assay were performed using the Line Gene 9620 software. Each fluorescent reporter signal was measured against the internal reference dye signal to normalize against non-PCR-related fluorescence fluctuations between wells. All samples were analyzed in triplicate independent experiments. All primers were synthesized by Ruibiotech. Co., Ltd.

Measurement of Hydroxyproline Amount

The measurement of hydroxyproline was conducted with a hydroxyproline measurement kit (NanJing JianCheng Bioengineering Institute) according to the manufacturer's instructions. Approximately 30 mg (wet weight) lung tissue was collected, 1 mL of alkaline hydrolysate was added, and the tissue was boiled at 95°C for 20 min with constant mixing. The pH was adjusted to 6.0-6.8 using the reagent provided. Approximately 3-4 mL of supernatant was collected for measurement after sorption onto active carbon. The hydrolysate was centrifuged at 3500 rpm for 10 min. Approximately 1 mL of supernatant was then carefully taken for measurement according to the manufacturer's instructions.

Analysis of Cellular Uptake of Peptides

Mouse AMs were treated with the indicated concentrations of FAM-conjugated peptides for the indicated time. The intracellular peptides were detected by confocal microscopy (Zeiss).

RNA Interference

Cells were transfected with specific siRNA oligonucleotides targeting GSK-3β (RIBOBIO). The sequences of GSK-3β-siRNAs were as follows: GSK-3β- siRNA1 sense, CCAUCAAGAAAGUUCUACAtt; GSK-3β-siRNA1 antisense, UGUAGAACUUUCUUGAUGGtt; GSK-3β-siRNA2 sense, CGACUGCGGUAU UUCUUCUtt; GSK-3β-siRNA2 antisense, AGAAGAAAUACCGCAGUCGtt. The delivery of siRNAs into cells was carried out with Lipofectamine RNA iMAX Transfection Reagent (Life Technologies) following the manufacturer's instructions. At 24-48 hr. after transfection, cells were collected for further analysis.

Analysis of Surface Plasmon Resonance

The binding kinetics between GSK-3β and the indicated peptides were measured by surface plasmon resonance using a BIAcore T200 instrument (GE Healthcare) as described previously (Hua et al., 2015). The dissociation constant (KD) was calculated with BIAevaluation software. The Langmuir module was used to determine the KD for all the peptides.

Plasmid Construction

The HA-tagged GSK-3β and truncation mutants of M1 (amino acids 1-123), M2 (amino acids 124-353), M3 (amino acids 124-433), and M4 (amino acids 1-353) were cloned into pCDNA3.1 vectors (Invitrogen) by a standard subcloning procedure. Myc-tagged A20 in a pReceiver-M43 vector was obtained from GeneCopoeia. The truncation mutants of A20, M1 (amino acids 1-1110) and M2 (amino acids 1111-2370) were cloned into the pCDNA3.1 vector (Invitrogen) by a standard subcloning procedure.

Macrophage Transfusion

Bronchoalveolar lavage fluids (BALF) from mice with multiple BLM exposures were centrifuged at 300 × *g* for 15 min. The pellets were resuspended and cultured in RPMI 1640 medium supplemented with 10% fetal bovine serum (FBS). After 2 hr, the adherent cells were scraped softly and resuspended in 50 μL of LPS-free PBS after centrifugation. Macrophages (2×10^6) were transfused intratracheally into normal mice a total of 6 times, with 7 days between each spray.

Three-dimensional Collagen Gels

Primary human lung fibroblast suspensions in serum-free medium were mixed with 3 mg/ml neutralized rat tail collagen type 1 at a ratio of 2:1. Then, cell suspensions at a density of 2×10^5/ml were seeded in 24-well plates, and the collagen gel was allowed to coagulate at 37°C for 1 hr before 1 mL of medium was added, and the edge of the gel was detached from the well walls. After 48 hr, images of the gels were taken, and the gel area was measured using ImageJ software (US National Institutes of Health).

Cycloheximide Treatment

To determine the amount of protein degradation, cells were incubated with 10 μg/ml protein synthesis inhibitor cycloheximide (CHX) for the indicated times, and the expression of the indicated proteins was evaluated by immunoblotting and quantitative analyses.

RNA Sequencing and Analysis

To detect changes in RNA in C/EBPβ -overexpressing AMs in the absence or presence of A20, the macrophages were transfected with Ad-*Cebpb* or Ad-*Cebpb* together with Ad-*Tnfaip3* for 24 hr. Total RNA was obtained, and RNA quantity and quality were measured with a NanoDrop ND-1000. Libraries were constructed according to standard Illumina protocols. The quality of the RNA and complementary DNA was monitored using an Agilent Bioanalyzer 2100, and sequencing was performed on an Illumina HiSeq 4000 by KangChen Biotech Company. The GEO accession number is GEO: GSE117690 in this study.

In Vitro Phosphorylation Assay

For the *in vitro* phosphorylation assay, low dose (0.5 mg) or high dose (1 mg) recombinant kinase (His-GSK-3β) and 2 mg of A20 were added to a 20 mL reaction containing 25 mM Tris (pH 7.5), 10 mM $MgCl_2$, 1 mM DTT, and 0.2 mM ATP. The reaction was incubated at room temperature (25°C) for 1 hr and terminated with SDS sample buffer. Protein mixtures were separated on SDS-PAGE with Phos-tag reagent, and A20 phosphorylation was detected with an anti-A20 antibody.

Flow Cytometry Analysis

The macrophages isolated from patient alveolar lavage fluid were treated with different doses of PA for 12 hr, and the cells were then softly scraped and centrifuged at 500 × *g* for 10 min. The pellets were resuspended in 100 μL of PBS. FBS (5%) was added, and the suspension was incubated for 45 min. Except for those in the negative group, the cells were stained with PE anti-mouse F4/80 and FITC anti-mouse CD206 for 45 min on ice in the dark. Then, the cells were washed with PBS before flow cytometry analysis. For the detection of intracellular proteins, the cells were first fixed with 4% paraformaldehyde for 15 min at room temperature, and 0.1% saponin was added to permeabilize the membranes for 5 min before incubation for background elimination.

QUANTIFICATION AND STATISTICAL ANALYSIS

All the statistical analysis was performed using Prism 6 (GraphPad Software). Data are expressed as the mean ± standard error of the mean (SEM). Statistical significance was evaluated by Student's t test or one-way ANOVA. Asterisk coding is indicated in the figure legends as *$p < 0.05$; **$p < 0.01$; ***$p < 0.001$. Statistical parameters including number of biological replicates and repeat experiments are reported in the figure legends.

DATA AND CODE AVAILABILITY

The accession numbers for the data reported in this paper are GEO: GSE117690 and SRA: SRR10007823 and SRR10007824.